Continuous-wave Raman laser in H2 : semi-classical theory and diode-pumping experiments
by Lei Stone Meng

A dissertation submitted in partial fulfillment of the requirements for the degree of Doctor of Philosophy in Physics
Montana State University

Abstract:
The far-off-resonance continuous-wave Raman laser is studied both theoretically and experimentally in this thesis. A semi-classical theory is developed for the far-off-resonance intracavity Raman proces's. Pumped by diode lasers in high-pressure H2 gas, our experiments achieve wide tunability and high conversion efficiency of the vibrational Stokes output. The theory agrees well with the experimental data in the steady state. In addition to the vibrational Stokes output, the rotational Stokes emission is also obtained in the experiments.

The cw Raman laser with anti-Stokes emission is theoretically studied. If all the three fields (pump, Stokes, and anti-Stokes) can be resonant with the cavity, significant cw anti-Stokes output is predicted.

In addition, longitudinal-mode bistability and mode-hop hystersis in the rotational Stokes laser are experimentally observed. A theory based on a Raman-assisted multi-wave mixing process successfully explains the observation.

CONTINUOUS-WAVE RAMAN LASER IN H_2: SEMI-CLASSICAL THEORY AND DIODE-PUMPING EXPERIMENTS

by

Lei Stone Meng

A dissertation submitted in partial fulfillment
of the requirements for the degree

of

Doctor of Philosophy

in

Physics

MONTANA STATE UNIVERSITY
Bozeman, Montana

August 2002

APPROVAL

of a dissertation submitted by

Lei Stone Meng

This dissertation has been read by each member of the dissertation committee and has been found to be satisfactory regarding content, English usage, format, citations, bibliographic style, and consistency, and is ready for submission to the College of Graduate Studies.

John L. Carlsten _____ 8-29-02
(Signature) Date

Approved for the Department of Physics

John C. Hermanson _____ 8.29.02
(Signature) Date

Approved for the College of Graduate Studies

Bruce R. McLeod _____ 8-30-02
(Signature) Date

STATEMENT OF PERMISSION TO USE

In presenting this dissertation in partial fulfillment of the requirements for a doctoral degree at Montana State University, I agree that the Library shall make it available to borrowers under rules of the Library. I further agree that copying of this dissertation is allowable only for scholarly purposes, consistent with "fair use" as prescribed in the U. S. Copyright Law. Requests for extensive copying or reproduction of this dissertation should be referred to Bell & Howell Information and Learning, 300 North Zeeb Road, Ann Arbor, Michigan 48106, to whom I have granted "the exclusive right to reproduce and distribute my dissertation in and from microform along with the non-exclusive right to reproduce and distribute my abstract in any format in whole or in part."

Signature 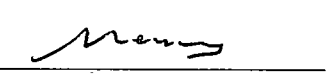

Date 8/30/02

ACKNOWLEDGEMENTS

First, I would like to thank my advisor, John Carlsten. With almost zero lab skills and poor English, I started my graduate work in John's lab. Without John's extremely patient guidance and support, I could not finish graduate school. Working with John has been a wonderful, and probably the most important experience of my life.

I would like to thank Kevin Repasky, Gregg Switzer, and Jay Brasseur who helped me get started in the lab. Thanks also go to Peter Roos, my coworker and labmate, who gave me many guiding thoughts and discussions. Thanks are also due to those people who helped me: Norm Williams, Peter Sellin, Tom Böttger and Xiaoguang Sun. In addition, I want to thank the rest of my fellow group members, Sytil Murphy and Yihan Xiong for our pleasurable moments in the lab.

Finally, I would like to thank my family; love goes to my parents for their support from far-away China.

TABLE OF CONTENTS

LIST OF TABLES vii

LIST OF FIGURES viii

ABSTRACT xix

1. INTRODUCTION 1

2. SEMI-CLASSICAL THEORY 7

Intracavity Field Equations 7
Maxwell's wave equation and the slowly varying envelope approximation 8
Spatial-mode expansion 9
Density Matrix Equations 11
Theoretical model and Schrödinger equation 11
Adiabatic elimination of C_j 15
Density-matrix equations 17
The polarization 18
The Stokes Laser 18
Population and coherence 19
Polarization and Raman gain 22
Intracavity field equations 25
Field amplitude equation and the steady-state oscillation condition 29
Frequency pulling 30
In terms of pump and Stokes powers 33
Numerical time-dependent solution 36
The Anti-Stokes Emission 42
Complex field equations 42
Analytic steady-state solution for zero two-photon-detuning 47
Numerical solution 50
Bad news: the dispersion 58

3. DIODE-PUMPED CW VIBRATIONAL RAMAN LASER 63

System Overview and Characteristics 63
Vibrational Raman transition in H_2 63
Threshold and steady-state power dependence 66
Stokes conversion efficiency and cavity impedance-matching 71
Tuning characteristics 75
Experiments 82
ECDL pumped, widely tunable 82
Highly efficient cw vibrational Raman laser 89

4. DIODE-PUMPED CW ROTATIONAL RAMAN LASER 98

Rotational Raman Transition in H_2 98
Introduction 98
Rotational Raman linewidth 99
Rotational Raman gain 101
Polarization dependence 104
Experiment 104
Etalon Effect of the Cavity Mirrors 110

5. MODE-HOP HYSTERESIS IN THE ROTATIONAL RAMAN LASER 115

Experimental Observation and Qualitative Explanation 115
Theory 122

6. SUMMARY 135

APPENDICES 137

APPENDIX A — LASER LOCKING 138

The Error Signal 139
The Electronics 142

APPENDIX B — MATHEMATICA PROGRAM 146

REFERENCES CITED 160

LIST OF TABLES

Table Page

1. Calculated frequency-offset values of the anti-Stokes cavity resonance caused by the dispersion (all for room temperature). Refractive indexes of H_2 are estimated by curve-fitting the published values given in reference [1]; page 6-95 61

2. Relative rotational Raman gains for different polarization conditions. .. 104

LIST OF FIGURES

Figure Page

1. Energy level diagram of the far-off-resonance Raman process. 1

2. Energy levels and laser fields for the far-off-resonance Raman process. The lowest level a is the ground state and the higher level b can be either a vibrational state or a rotational state. We allow an arbitrary number of higher level j and all possible orders of Stokes and anti-Stokes [labeled by an integer q and here only shows $q = \pm 1$ ($q = 0$ is the pump)] generated by the Raman process for the most generality. The transition between levels a and b is electric dipole forbidden. The transitions $j \leftrightarrow a$ and $j \leftrightarrow b$ are far off single-photon resonances and there may be a two-photon detuning δ for the $a \leftrightarrow b$ transition ($\delta < 0$ in the configuration shown). 12

3. Energy levels and laser fields for the Stokes laser. Level a is the ground state; level b can be either a vibrational state or a rotational state; levels denoted by j are multiple excited electronic states. The pump field ω_p ($q = 0$) is red-shifted to the Stokes field ω_s ($q = -1$) and a molecular coherence $\rho_{ab}e^{i\omega_m t}$ is established between levels a and b. There can be a two-photon detuning denoted by δ. 19

4. Raman plane-wave gain coefficient as a function of the two photon detuning. For the vibrational Raman transition (792→1180 nm, solid line), $\alpha_{gv}(0) = 1.5 \times 10^{-11}$ m/W [2], linewidth (HWHM) $\gamma_{abv}/2\pi =$ 250 MHz [3]. For the rotational transition (792→830 nm, dashed line), $\alpha_{gr}(0) = 0.5 \times 10^{-11}$ m/W [4, 5, 6], linewidth (HWHM) $\gamma_{abr}/2\pi =$ 510 MHz [7]. Gain and linewidth are for 10 atm H_2 at 300 K room temperature. 25

5. Theoretical calculation of the amount of frequency-pulling $\dot{\phi}$ as a function of two-photon-detuning δ in a cw vibrational Raman laser. Solid line: pump; dashed line: Stokes. Parameters used are: $\lambda_p = 792$ nm; $\lambda_s = 1180$ nm; $\alpha_g = 1.5 \times 10^{-9}$ cm/W (line-center value for 10 atm H_2 at 25°C); mirror transmittance = 0.9999; mirror absorption = 30×10^{-6}; cavity length = 7.62 cm; and pumping rate is at four times the line-center threshold. In the two shaded areas, the Stokes laser is below threshold. 33

6. Numerical simulation of the "turn-on" behavior in a cw vibrational Raman laser at different pumping rates. The pump (top) and the Stokes (bottom) powers are plotted as functions of time. The solid line is at a pumping rate of 4 times the threshold; the dashed line is at 2 times the threshold; and the dotted line is at 1.2 times the threshold. All the curves are at the Raman gain line-center (i.e., the two-photon-detuning $\delta = 0$). The left horizontal axis is the intracavity spatial peak power and the right axis is the cavity transmitted power (single end). 37

7. Numerical simulation of the "turn-on" behavior in a cw vibrational Raman laser at different detunings. The pump (top) and the Stokes (bottom) powers are plotted as functions of time. The solid line is when the two-photon-detuning $\delta/2\pi = 0$; the dashed line is when $\delta/2\pi = 200\,\mathrm{MHz}$; and the dotted line is when $\delta/2\pi = 400\,\mathrm{MHz}$. All the curves are at the pumping rate of 4 times the line-center threshold. The left horizontal axis is the intracavity spatial peak power and the right axis is the cavity transmitted power (single end). 38

8. After the cw Raman laser in Fig. 7 grows into steady-state (note the horizontal time scale), the calculated phase evolutions of the pump (top) and the Stokes (bottom) beams are shown for different detunings. The slope of the phase curve gives the amount of frequency-pulling. 40

9. The slopes of the phase curves in Fig. 7 as functions of the two-photon-detunings. This numerical calculation agrees with the theoretical plot in Fig. 5. 41

10. The values of $\mathrm{sinc}(\Delta kL/2) = \frac{\sin(\Delta kL/2)}{\Delta kL/2}$ as a function of cavity length. We plotted for $\lambda_p = 792$ nm, $\lambda_s = 830$ nm in the rotational transition and $\lambda_s = 1180$ nm in the vibrational transition at two different H_2 pressures. When the H_2 pressure is 10 atm (3 atm), $\Delta k \approx -4.6\mathrm{m}^{-1}(-1.4\mathrm{m}^{-1})$ for the rotational transition and $\Delta k \approx -54\mathrm{m}^{-1}(-16\mathrm{m}^{-1})$ for the vibrational transition. 7.62 cm (3 in) is the cavity length we have used in the demonstrated cw Stokes laser systems. 46

11. Values of ξ's are calculated as function of cavity length (left: ξ_-, right: ξ_+). ξ_+ is always larger than 1. 7.62 cm (3 in) is the cavity length we have used in the demonstrated systems. Parameters used for calculation are: $\lambda_p = 792$ nm, $\lambda_s = 830$ nm, $\lambda_a = 757$ nm (rotational), $\lambda_s = 1180$ nm, $\lambda_a = 596$ nm (vibrational), reflectance and absorption are 0.9999 and 30 ppm for both mirrors and all wavelengths, mirror radius of curvature is 50 cm, H_2 pressure is 10 atm, and $\Delta k \approx -4.6\,\mathrm{m}^{-1}$ for the rotational transition, $\Delta k \approx -54\,\mathrm{m}^{-1}$ for the vibrational transition. 49

12. Theoretical plots for the rotational Raman laser (steady-state and zero two-photon-detuning). Thin curves are for the usual Stokes laser while thick curves are when there is four-wave mixing coupling between the Stokes and anti-Stokes. About 8.5% power conversion from Stokes to anti-Stokes, or 3.5% peak power conversion from the input pump to the anti-Stokes can be achieved. Same parameters are used for calculation as in Fig. 11. 50

13. Numerical simulation of the "turn-on" behavior in a cw rotational Raman laser with anti-Stokes emission at different Raman detunings. The pump (top), Stokes (middle), and anti-Stokes (bottom) powers are plotted as functions of time. They are all pumped at 4 times the line-center threshold (= 2.4 mW). The solid line, the dashed line, and the dotted line are when the two-photon-detuning $\delta/2\pi = 0$ MHz, = 400 MHz, and = 800 MHz respectively. The left horizontal axis is the intracavity spatial peak power and the right axis is the cavity transmitted power (single end)..... 53

14. The steady-state powers of pump (top), Stokes (middle), and anti-Stokes (bottom) are numerically calculated as functions of the two-photon-detuning. The solid line, the dashed line, and the dotted line are when the pumping-rate is equal to 2×, 4×, and 8× the line-center threshold (= 2.4 mW) respectively. The left horizontal axis is the intracavity spatial peak power and the right axis is the cavity transmitted power (single end)..... 54

15. The numerically calculated steady-state phase evolutions in a cw rotational Raman laser with anti-Stokes emission at different Raman detunings. The pump (top), the Stokes (middle), and the anti-Stokes (bottom) phases are plotted as functions of time. They are all pumped at 4 times the line-center threshold (= 2.4 mW). The solid line, the dashed line, and the dotted line are when the two-photon-detuning $\delta/2\pi = 0$ MHz, = 400 MHz, and = 800 MHz respectively..... 55

16. The numerically calculated steady-state frequency-pullings of pump (top), Stokes (middle), and anti-Stokes (bottom) as functions of two-photon-detuning. The solid line, the dashed line, and the dotted line are when the pumping-rate is equal to 2×, 4×, and 8× the line-center threshold (= 2.4 mW) respectively. The random noise-like curves are when the laser is below threshold. 56

17. The numerically calculated phase difference, $\Delta\phi = 2\phi_p - \phi_s - \phi_a$, as a function of time. The solid line, the dashed line, and the dotted line are when the two-photon-detuning $\delta/2\pi = 0$ MHz, = 400 MHz, and = 800 MHz respectively. They are all pumped at 4 times the line-center threshold (= 2.4 mW). 57

18. The numerically calculated steady-state values of the phase difference, $\Delta\phi = 2\phi_p - \phi_s - \phi_a$, as a function of two-photo-detuning. The solid line, the dashed line, and the dotted line are when the pumping-rate is equal to 2×, 4×, and 8× the line-center threshold (= 2.4 mW) respectively. 57

19. Illustration of (single-photon) dispersion effect in a high-finesse Raman cavity. Solid vertical lines represent actual cavity longitudinal modes (the taller and thicker solid lines means the oscillating modes); dotted vertical lines are "conceptual" and are drawn equally spaced — they are the longitudinal modes assuming that the intracavity refractive index is a constant n_p. Using these modes as a reference, the actual cavity mode-spacings will be larger at lower frequencies and smaller at higher frequencies. ν_{ab} is the Raman shift; Δ is the Raman detuning of the lasing Stokes mode; Δ' is the detuning of the anti-Stokes resonance. The anti-Stokes mode cannot oscillate unless $\Delta' = -\Delta$. 58

20. Dispersion in Raman cavity. Refractive index values are for rotational Raman transition (pump = 792 nm, Stokes = 830 nm, and anti-Stokes = 757 nm) in 10 atm H_2 at room temperature. Δn and $\Delta n'$ are the average index changes per free-spectral-range. 60

21. Energy level diagram for the cw vibrational Raman laser in H_2. Spectral distances between levels and laser frequencies are drawn to scale. a, Three levels from bottom to top are (thick solid lines): the ground state, the first vibrational state, and the first excited electronic state. Distance between the ground state and the first electronic state is about 90,000 cm^{-1}. b, Zoomed-in diagram showing the two-photon Raman process. The incident pump photon transfers population from the ground state (the vibrational quantum number $v = 0$) to the vibrational state $v = 1$ producing a Stokes photon with a frequency shift of 4155 cm^{-1} 63

22. Vibrational Raman gain linewidth and peak plane-wave gain coefficient in H_2 as functions of pressure at 25°C. A pump wavelength of 792 nm is used in calculating the gain coefficient. 65

23. Theoretically calculated intra-cavity pump and Stokes spatial peak powers as functions of input pump power. This is calculated for the vibrational Stokes emission (1180 nm) pumped by 792 nm laser and the Stokes cavity resonance is in the gain line-center. Cavity finesse is assumed to be 31,400 ($R = 0.9999$) at both wavelengths. 68

24. Theoretically calculated optical powers measured outside the cavity as functions of input pump power. The calculation parameters are the same as used in Fig.23. We add the Stokes powers in front and back of the cavity to obtain the total Stokes power. 70

25. Theoretically calculated photon conversion efficiency as a function of input pump power. The top x axis labels the pumping rate normalized to the laser threshold. Parameters for calculation are the same as used in Fig.23. Photon conversion efficiency reaches the maximum value at 4 times threshold. 71

26. Various optical fields associated with a high-finesse Raman cavity. Field 1: input pump; 2: directly-reflected pump field from the front mirror; 3: cavity leakage pump field; 4: cavity leakage Stokes field; 5: intra-cavity pump field; 6: intra-cavity Stokes field. Field 2 and 3 have 180° phase difference; thus the total reflected pump field is the destructive interference between these two fields. 72

27. Behaviors of asymmetric pump cavity ($R_{1p} = 0.998$, $R_{2p} = 0.9999$) predicted by the theory. a, Stokes and pump fields as functions of input pump power; b, photon conversion efficiency as a function of input pump power. Above the threshold (3.3 mW), the reflected pump power decreases to approach the impedance-matched condition. The Stokes photon conversion efficiency reaches a maximum value of $\sim$ 66% at four times threshold. Ideally, if we let all the mirror losses be zero and $R_{2p} = 1$, 100% photon conversion efficiency can be reached (dotted line in b). 74

28. Picture of cavity longitudinal modes in a cw Raman laser and how the Stokes field chooses a lasing mode. Frequency distance ν_{ab} between pump and Stokes gain line-center is the Raman shift. $c/2L$ is the cavity longitudinal mode spacing or the free-spectral-range (c: light speed, L: cavity length). This cavity mode picture was first viewed by Roos. 75

29. Tuning picture of the cw Raman laser. Initially the Stokes cavity resonance ν_s has an arbitrary detuning of Δ_0 away from the Raman gain line-center. As the pump frequency ν_p is tuned by $\delta\nu_p$, the Stokes gain line-center is tuned by the same amount. However the frequency change of the Stokes cavity resonance is smaller: $\delta\nu_s < \delta\nu_p$. Thus in this picture the Stokes resonance will be tuned closer to the Raman gain line-center. 76

30. The gain "seen" by three adjacent longitudinal Stokes modes as the pump laser's frequency is tuned. The Stokes longitudinal mode-spacing is assumed to be 2 GHz. For the center Stokes mode, we assume its initial detuning $\Delta_0 = 0$ when $\delta\nu_p = 0$. 78

31. Tuning characteristics of the cw Raman laser in symmetric pump cavity. We calculate the total Stokes power (top), the transmitted pump power (middle) and the reflected pump power (bottom) as functions of the pump frequency tuning. Four different pumping rates, 2×, 4×, 8×, and 16× the line-center threshold are plotted. Parameters used for calculation are the same as those used in Fig. 24 and 25. 79

32. Tuning characteristics of the cw Raman laser in asymmetric pump cavity. Parameters used for calculation are the same as those used in Fig. 27. 80

33. Experimental setup of the ECDL-pumped vibrational Raman laser. ECDL: external-cavity diode laser; APP: anamorphic prism pair; MML: mode-matching lenses; EOM: electrooptic modulator; $\frac{\lambda}{2}$: half-wave plate; PBS: polarizing beam splitter; $\frac{\lambda}{4}$: quarter-wave plate; HFC: high-finesse cavity; PBP: Pellin-Broca prism. 84

34. Experimental data of the ECDL-pumped vibrational Raman laser. The Stokes power and the transmitted pump power are measured as functions of the input pump power. The lines are the theoretical fits. .. 86

35. Photon conversion efficiency as a function of input pump power. The maximum efficiency is $(12.0 \pm 1.3)\%$ occurring at four times threshold.. 87

36. Tunability of the ECDL-pumped vibrational Raman laser. The 18 nm wavelength of the pump beam (top) results in a 40 nm discretely tunable Stokes beam (bottom). The wavelength measurements were taken with a HP optical spectrum analyzer (resolution: 0.1 nm)..... 88

37. Continuous tuning of the ECDL-pumped vibrational Raman laser. The Stokes power is measured when the pump frequency is tuned (bottom horizontal axis; the Stokes frequency change is shown by the top horizontal axis). We take the measurements at five different pumping rates: 2×, 4×, 8×, 16×, and 26× the line-center threshold. The Stokes can be continuously tuned by about 1.3 GHz..... 89

38. Experimental setup of a highly efficient cw vibrational Raman laser. The pump laser is a broad-area diode laser (BADL) injection-locked by an external-cavity diode laser (ECDL). APP: anamorphic prism pair; $\frac{\lambda}{2}$: half-wave plate; MML: mode-matching lenses; EOM: electrooptic modulator; PBS: polarizing beam splitter; $\frac{\lambda}{4}$: quarter-wave plate; HFC: high-finesse cavity. 91

39. Geometry of the injection into the slave BADL diode. The BADL's facet size is 100×1 μm. It has been experimentally discovered [8, 9] that the best injection-locking performance is achieved when (1)the master beam is injected into one edge of the BADL front facet by an incident angle of 3-4° and (2) the beam waist diameter is 1/2 width of the front facet area (50×1 μm). 92

40. BADL injection-locking results. a, Spectra of BADL's output measured by an optical spectrum analyzer (resolution 0.1 nm) when free-running and injection-locked. b, When injection-locked, the transimitted signal from the scanning Raman HFC (without H_2). The HFC's free-spectral-range is 2 GHz; its linewidth is ~1 MHz. 93

41. Experimental data of the BADL-pumped vibrational Raman laser. a, The Stokes power and the transmitted pump power are measured as functions of the input pump power. b, Photon conversion efficiency as a function of the input pump power. Curves are the theoretical fits. The deviations between the data and the theory are caused by the thermal lens effect of the Raman gas [10]..... 95

42. Energy levels in H_2 showing transitions for both vibrational (1180nm) and rotational (830 nm) Stokes pumped with 792 nm. At room temperature of 300 K and a H_2 pressure of 10 atm, the FWHM Raman gain linewidth of the vibrational transition $Q_{01}(1)$ is $\Gamma_v = 0.5$ GHz and the rotational transition $S_{00}(1)$ has $\Gamma_r = 1.02$ GHz. 98

43. Rotational and vibrational Raman linewidth in H_2 as functions of pressure or density at 295 k. 0.146 atm (0.134 amagat) is the cutoff pressure (density) for the rotational transition, below this density, the rotational linewidth is dominated by Doppler-broadening and Eq. (4.1) cannot be applied. The cutoff density for the vibrational transition is 1 amagat..... 100

44. Rotational and vibrational Raman gain in H_2 as functions of pressure or density at room-temperature (295-300 K). Both are calculated for the pump wavelength of 792 nm. The rotational gain is for circularly polarized pump light and counter-circularly polarized Stokes output; while the vibrational gain is independent of pump polarization. 103

45. Experimental setup of the ECDL-pumped rotational Raman laser. ECDL: external-cavity diode laser; $\frac{\lambda}{2}$: half-wave plate; PBS: polarizing beam splitter; EOM: electrooptic modulator; SM-PM fiber: single-mode and polarization-maintaining fiber; MML: mode-matching lens; $\frac{\lambda}{4}$: quarter-wave plate; HFC: high-finesse cavity. 105

46. Continuous-tuning data measured from the setup in Fig. 45. 106

47. Power dependences measured from the setup in Fig. 45. 106

48. HFC-mirror transmittance trace provided by the mirror-coating manufacturer (Research Electro-Optics, inc.). The double-wavelength coating at 792 and 1180 nm is originally manufactured for the cw vibrational Raman laser, but the wide coating bandwidth also covers the rotational wavelength at 830 nm. 107

49. (a) The Raman plane-wave gain coefficients associated with the vibrational and rotational Stokes cavity modes as functions of the pump frequency tuning. The cavity resonances of both Stokes are assumed to be at the gain line-center when the relative pump frequency is zero (i.e., Δ_0=0). (b) Based on these gain profiles, calculation of the power of the transmitted pump, the rotational Stokes, and the vibrational Stokes as functions of pump tuning. Parameters used for the calculation are: mirror reflectances: 0.9999; mirror absorptions: 40 ppm at all wavelengths and both mirrors; input pump power: 5 mW. The range shown is in qualitative agreement with the measure data presented in Fig. 46. 108

50. Illustration of the etalon effect of the HFC mirrors. The uncoated back surfaces have reflectances of about 0.034, given by the refractive index of fused silica: 1.4534 (800 nm) [1, page6-25]..... 111

51. Cavity reflected and transmitted laser power (normalized to the coupled input power) as functions of the incident laser's frequency. The incident laser's power remains at ~5.3 mW and the cavity coupling efficiency is estimated to be ~85%. The laser frequency is measured relative to 378 600.00 GHz by a Burleigh wavemeter with 10 MHz resolution. Because the two cavity mirrors are actually two etalons, the mirrors' effective reflectance is a function of the laser's frequency and this results in periodic reflected and transmitted laser power from the HFC. The curves are fittings assuming sinusoidal effective reflectances (see Fig. 52) of the HFC mirrors..... 111

52. Comparison between the sinusoidal effective-reflectances which fit the data and the calculated effective-reflectances based on the etalon model. 114

53. Experimental data showing the mode-hop hysteresis between the two adjacent rotational Stokes modes. Optical frequencies are measured by a Burleigh wavemeter with 10 MHz resolution. The pump frequency is measured relative to 378 350 GHz and the Stokes frequency is measured relative to 360 750 GHz. 116

54. Transmitted pump power (top) and rotational Stokes power (bottom) as functions of pump frequency tuning show butterfly-like patterns. Power discontinuities indicate mode-hops. The input pump beam is circularly polarized and the rotational Stokes is counter-circularly polarized for both modes [11]. The pump frequency tuning is shown relative to 378 384 GHz. Back and forth tuning of the pump frequency is performed twice..... 117

55. Picture showing how the mode-hop hysteresis happens. $\delta(<0)$ and $\delta_+(>0)$ are the two-photon-detunings of the rotational Stokes modes ω_s and ω_{s+} respectively. $\Delta_c = \delta_+ - \delta$ is the longitudinal mode spacing of the two Stokes modes. The width of the rotational Raman gain linewidth is sufficient to cover the two adjacent longitudinal Stokes modes. a, The "symmetric point", where the two Stokes modes lie symmetrically away from the line-center, $|\delta| = |\delta_+|$. The sub-threshold mode ω_{s+} loses some gain so it is below threshold. b, The mode-hop point, where $|\delta| > |\delta_+|$ and the mode ω_{s+} reaches the threshold since it is closer to the line-center and the lost gain is compensated. c, After the mode-hop, the steady-state gain is quickly saturated to a lower level so that the mode ω_{s+} sees equal gain and loss. 118

56. Theoretical model for mop-hop hysteresis. a, The usual Raman process: the pump field at frequency ω_p and the lasing-Stokes mode at frequency ω_s estabish a strong coherence between the two energy states oscillating at frequency $\omega_m = \omega_p - \omega_s$. b, The first FWM process: the sub-threshold Stokes $\omega_{s+} = \omega_s + \Delta_c$ beats with the strong pump ω_p, producing a weak coherence sideband oscillating at $\omega_p - \omega_{s+} = \omega_m - \Delta_c$; then the lasing-Stokes mode is scattered off this coherence sideband to produce a weak pump sideband with frequency $\omega_{p-} = \omega_p - \Delta_c$. c, The second FWM process (a and c together): the sub-threshold Stokes ω_{s+} is scattered off the strong coherence, producing another new weak field ω_{p+}. d, A "bonus" new weak field is generated, although it does not contribute to the gain suppression on ω_{s-}: the sideband ω_{p-} is scattered off the strong coherence, producing a new field ω_{s+}. In this plot, we use the thick lines to represent "strong" and the thin lines mean "weak". 120

57. Plot of $f(\delta, R')$ as a function of the two-photon detuning at 3 different pumping rates. $f(\delta, R') = 0$ is when mode-hop should happen. $\delta_1/2\pi = -\Delta_c/2 = 0.985\,\text{GHz}$ (cavity length $= 3\,\text{inch}$) is the symmetric point — there is no hysteresis when the laser is pumped right at the threshold. As the laser is pumped harder, we see $\delta_2 > \delta_{1.5} > \delta_1$ — the higher the pumping level, the larger the hysteresis. 132

58. Plot of H as a function of the pumping rate R'. Circles are the experimental measurements. 133

59. Illustration of the Pound-Drever-Hall laser stabilization technique. EOM: electrooptic modulator; PBS: polarizing beam splitter; $\frac{\lambda}{4}$: quarter-wave plate. 139

60. Calculated error signal shape from Eq.(6.11) when either the laser frequency ω_L or the cavity length L is scanned. The in-phase signal is obtained when $\Delta\phi = 0$; the quadrature signal is when $\Delta\phi = \pi/2$. Following parameters are used in calculation: modulation frequency: 12 MHz; mirror reflectance: 0.998 for both mirrors; laser wavelength: 792 nm; cavity length: 7.62 cm. 142

61. Electronic circuit diagram of the EOM driver and phase shifter. It can produce rf sine wave to two output channels. Relative phase of the two channels is adjustable. 144

62. Electronic circuit diagram of the error signal amplifier. It has variable gain (5kΩ pot) and adjustable dc offset (20kΩ pot). 145

ABSTRACT

The far-off-resonance continuous-wave Raman laser is studied both theoretically and experimentally in this thesis. A semi-classical theory is developed for the far-off-resonance intracavity Raman process. Pumped by diode lasers in high-pressure H_2 gas, our experiments achieve wide tunability and high conversion efficiency of the vibrational Stokes output. The theory agrees well with the experimental data in the steady state. In addition to the vibrational Stokes output, the rotational Stokes emission is also obtained in the experiments.

The cw Raman laser with anti-Stokes emission is theoretically studied. If all the three fields (pump, Stokes, and anti-Stokes) can be resonant with the cavity, significant cw anti-Stokes output is predicted.

In addition, longitudinal-mode bistability and mode-hop hystersis in the rotational Stokes laser are experimentally observed. A theory based on a Raman-assisted multi-wave mixing process successfully explains the observation.

CHAPTER 1

INTRODUCTION

The continuous-wave (cw) Raman laser is a recently developed laser technique for generating tunable high-quality laser beams in the near-infrared. It is based on stimulated Raman scattering as illustrated in Fig. 1.

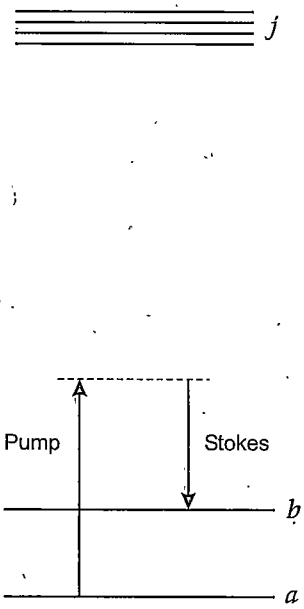

Figure 1 Energy level diagram of the far-off-resonance Raman process.

Level a in Fig. 1 is the ground state, level b is the molecular vibrational or rotational state, and the levels marked j are the excited electronic states. The transition between levels a and b is electric dipole forbidden. Raman scattering occurs when an incident photon (called the pump) interacts with the molecule and generates a

red-shifted photon (called the Stokes). When the intensity of the pump laser is high enough to reach some certain threshold, the Stokes output experiences significant amplification (appearing as exponential growth) and this is called stimulated Raman scattering (SRS). Note that for the 792 nm pump wavelength we will be using in this thesis, the transitions $j \leftrightarrow a$ and $j \leftrightarrow b$ are far off single-photon electronic resonance and therefore we call the Raman scattering in Fig. 1 the "far-off-resonance" Raman process.

Because of this far-off-resonance condition, the gain of the SRS is very low. The SRS threshold is in the range of 10^2–10^3 kW of pump power. Therefore traditionally, the SRS is usually associated with high power pulsed lasers. For example, in a review paper written by Bloembergen in 1967 [12], it was said: "The general background for the development of the field of stimulated Raman emission contained the following factors: ...the development of high-power pulsed solid-state lasers."

Because of the lower intensity of cw pump lasers, to realize SRS in the cw regime, the low Raman gain has to be enhanced in some way. One technique is called resonance enhancement [13, page 101]: the cw pump laser and the Raman medium are chosen so that the pump frequency is near a molecular or atomic resonance. The Raman gain is usually large when near resonance but the drawback is that the SRS is tunable only in the very narrow regions near resonance. Many near-resonance cw Raman lasers have been developed over the last 2-3 decades (for example, references [14] and [15]).

In this thesis, when speaking of a "cw Raman laser", we refer to a far-off-resonance cw Raman laser exclusively. Instead of resonance enhancement, we utilize high-finesse-cavity enhancement — performing SRS in a high finesse cavity. Currently mirror coating technology is able to manufacture low loss (< 15 ppm) mirrors with high reflectances ($> 99.99\%$). With these mirrors, we are able to build Fabry-Perot cavities with finesses of 10^4 and higher. Furthermore, the mirrors can be doubly coated and the finesses of $> 10^4$ can be realized at both the pump and Stokes wavelengths. Through the use of this double-cavity-enhancement, it can be shown that a SRS threshold of 200 kW can be effectively lowered to 0.8 mW (see page 68). This is an order of 10^8 enhancement and the result is that cw diode laser pumping is fully possible.

The first far-off-resonance cw Raman laser was realized by Brasseur *et al.* in 1998 [16]. Diatomic hydrogen gas (H_2) was used as the Raman gain medium and the pump laser was a frequency-doubled Nd:YAG laser. Roos *et al.* then demonstrated the first diode-pumped cw Raman laser, using a free-running diode laser and a passive optical locking technique [17]. The Stokes laser threshold was as low as 240 μW. Shortly after, an external-cavity-diode-laser(ECDL)-pumped cw Raman laser succeeded [18]. The Stokes output of this system was able to be tuned over a wide 40 nm range due to the tunability of the ECDL. Next, by improving the cavity impedence-matching, another diode-pumped cw Raman laser was demonstrated to have a high photon-conversion-efficiency of 66% [19, 20]. The latest achievement on the cw Raman laser

was the discovery of the rotational Stokes emission in H_2 [11], while all the above demonstrations were based on the vibrational Raman transition in H_2.

There are several distinguishing features associated with the cw Raman laser. First, the Stokes output is widely tunable because the far-off-resonance condition leads to flat gain over a wide spectral range. This wide tunability (tens of nanometers) is usually discrete due to the double cavity resonance requirement. But the Raman gain linewidth and the relative movement of the pump and Stokes resonances can bring us a continuous tuning range of 1-2 GHz for the vibrational transition and of >20 GHz for the rotational transition. Second, the Stokes output has a very narrow spectral linewidth. A linewidth of less than 10 kHz has been measured in the Nd:YAG-pumped system [21]. Third, the Stokes output also has a high spatial purity. The Stokes beam is a pure TEM_{00} fundamental Gaussian mode because of the output from the high-finesse non-confocal cavity.

In cw Raman lasers, phase matching is automatically satisfied since the dipole (or molecular coherence) is induced with the proper phase which leads to Stokes growth, independent of the phase relation between the laser and the Stokes waves. This is an advantage of the cw Raman laser compared to other techniques of laser frequency down-conversion, such as the optical parametric oscillator.

The cw Raman laser may provide a novel tool for studying Raman scattering itself. The traditional pulsed-laser-method has its own limitations on studying Raman scattering. For example, vibrational as well as rotational scatterings always appear

at the same time under many conditions, making independent studies on each type impossible. Just as Minck *et al.* wrote in a 1966 paper [22]: "Because in both D_2 and H_2 the vibrational transitions were always stimulated when the laser was plane polarized, it was not possible to measure the polarization dependence of threshold power for the rotational transitions." Now this difficulty can be easily solved in cw Raman lasers. As shown in Chapter 4, the double resonance requirement and the homogeneous gain nature of the Raman medium assures single-mode operation — pure vibrational Stokes or pure rotational Stokes can be selected just by tuning the pump laser's frequency.

The cw Raman laser also serves as a unique system for studying some aspects of basic laser physics, such as mode-mode competition and the resulting dynamics. For example, in Chapter 5 we report a mode-hop hysteresis and bistability observed in a cw rotational Raman laser. When two adjacent longitudinal laser modes lie symmetrically between the homogeneous gain line-center, the laser output shows a mode-hop hysteresis. To our knowledge, such a mode-hop hysteresis in a homogeneous laser has not been directly observed before.

Besides being a down-conversion technique, it is also possible to generate blue-shifted laser light (up-conversion) in a cw Raman laser system. This up-conversion is based on Stokes–anti-Stokes coupling. We will show theoretically that if the triple-resonance condition (i.e., the cavity is resonant simultaneously at the pump, Stokes, and anti-Stokes wavelengths) is satisfied, significant anti-Stokes light can be generated

with the threshold pump power lower than 10 mW (See Section 2).

The structure of this thesis is as follows. Chapter 2 gives the complete semi-classical theory for the cw Raman laser. Not only the Stokes lasing is described mathematically, but the anti-Stokes emission is studied theoretically as well. Both the analytical steady-state solution and the time-dependent numerical simulation are given for the Stokes and anti-Stokes equations. Chapter 3 – 5 give experimental achievements of the diode-pumped cw Raman lasers. The vibrational Stokes lasers are presented in Chapter 3, including general characteristics of the cw Raman laser, the ECDL-pumped system, and the broad-area-diode-laser(BADL)-pumped system. The discovery of the rotational Stokes emission is reported in Chapter 4, including an introduction to the rotational Raman transition, the experimental observations, and a practical issue regarding the cavity's etalon effect. The mode-hop hysteresis effect in the rotational Raman laser is studied in Chapter 5, in which our theoretical model successfully explains the hysteresis.

CHAPTER 2

SEMI-CLASSICAL THEORY

In this chapter, we develop a semi-classical theory for the far-off-resonance cw Raman laser. In the first Section we derive the cw field equations in a laser cavity. In the second Section we study the density matrix equations. Then in the third Section we discuss the cw Raman laser with first-order Stokes generation. Finally, the last Section solves the intracavity Stokes–anti-Stokes coupling.

The semi-classical theory for the single-mode Stokes laser was first developed by Brasseur [23, 21]. We derive his theory in this thesis more systematically and also extend it to a more general case — arbitrary number of intracavity fields. The intracavity Stokes–anti-Stokes coupling equations were derived by the great help from Roos. He solved the same problem fully quantum mechanically [24] and obtained the same results.

Intracavity Field Equations

In this section we derive the laser field equations in a standing-wave Fabry-Perot cavity. We first apply the slowly varying envelope approximation into the classical Maxwell's wave equation. We then separate the time and spatial dependence by a method of normal mode expansion. The references of these derivations are Siegman

[25], Brasseur [23], and Roos [24].

Maxwell's wave equation and the slowly varying envelope approximation

We start from Maxwell's wave equation[1] (in scalar form for simplicity):

$$\ddot{\tilde{E}}(\mathbf{r},t)+\frac{\sigma}{\epsilon_0}\dot{\tilde{E}}(\mathbf{r},t)-c^2\nabla^2\tilde{E}(\mathbf{r},t)=-\frac{1}{\epsilon_0}\ddot{\tilde{P}}(\mathbf{r},t), \tag{2.1}$$

where σ is the ohmic conductivity of the laser medium; ϵ_0 and c are the dielectric permeability and the light velocity of the free space; P is the total macroscopic polarization of the medium. The second term in the left-hand-side of the equation is used to simulate losses in a Fabry-Perot cavity. We suppose that there are multiple fields in the cavity:

$$\tilde{E}(\mathbf{r},t)=\frac{1}{2}\sum_q\left[E_q(\mathbf{r},t)e^{-i\omega_q t}+\text{c.c.}\right], \tag{2.2}$$

where the integer q will denote the various frequency components inside the cavity such as the pump and the Stokes fields in our later sections. It can also denote different longitudinal modes of the pump or the Stokes depending on the problem, as, for example, in the analysis of the mode-hop hysteresis in a rotational Raman laser in Chapter 5. We assume that the polarization density in the cavity can be written in the same form:

$$\tilde{P}(\mathbf{r},t)=\frac{1}{2}\sum_q\left[P_q(\mathbf{r},t)e^{-i\omega_q t}+\text{c.c.}\right]. \tag{2.3}$$

[1] Throughout this thesis, we use the tilde to denote a quantity that varies rapidly in time, while the slowly-varying amplitudes of Fourier components are written without the tilde.

There may also be external injected fields in the same form:

$$\tilde{E}_e(\mathbf{r},t) = \frac{1}{2}\sum_q \left[E_{eq}(\mathbf{r},t)e^{-i\omega_q t} + \text{c.c.}\right], \tag{2.4}$$

and the wave equation (2.1) is expanded to

$$\ddot{\tilde{E}}(\mathbf{r},t) + \gamma_c\dot{\tilde{E}}(\mathbf{r},t) - c^2\nabla^2\tilde{E}(\mathbf{r},t) = -\frac{1}{\epsilon_0}\ddot{\tilde{P}}(\mathbf{r},t) + \gamma_e\dot{\tilde{E}}_e(\mathbf{r},t), \tag{2.5}$$

where we introduce the notation γ_c to represent the intracavity energy decay rate due to primarily the losses of the mirrors, while γ_e represents the coupling rate of the externally injected energy.

Substituting these expansions (2.2)-(2.4) into the wave equation (2.5) and by making the slowly varying envelope approximation[25, page 945], we have for each field q:

$$\dot{E}_q(\mathbf{r},t) + \left[\frac{\gamma_{cq}}{2} - i\frac{1}{2\omega_q}(\omega_q^2 + c^2\nabla^2)\right]E_q(\mathbf{r},t) = i\frac{\omega_q}{2\epsilon_0}P_q(\mathbf{r},t) + \frac{\gamma_{eq}}{2}E_{eq}(\mathbf{r},t). \tag{2.6}$$

Here γ_{cq} and γ_{eq} are associated with cavity mirrors' reflectance R, transmittance T and cavity length L by (if we neglect the scattering loss inside the cavity)

$$\gamma_{cq} = -\frac{c}{n_q L}\ln\sqrt{R_{1q}R_{2q}}, \tag{2.7a}$$

$$\gamma_{eq} = \frac{2c}{n_q L}\sqrt{T_{1q}}, \tag{2.7b}$$

where n_q is the refractive index for the field q; the subscript "1" represents the front mirror that couples the external field E_{eq} and "2" means the back mirror.

Spatial-mode expansion

We next assume that each electric field q inside the cavity can be expanded in a set of normal spatial modes $u_n(\mathbf{r})$:

$$E_q(\mathbf{r},t) = \sum_n E_{q,n}(t)u_{q,n}(\mathbf{r}). \tag{2.8}$$

These modes are assumed to be solutions of Laplace's equation

$$(\nabla^2 + k_{cq,n}^2)u_{q,n}(\mathbf{r}) = 0 \tag{2.9}$$

which satisfy the boundary condition of the cavity. $k_{cq,n} = \omega_{cq,n}/c$, where $\omega_{cq,n}$ is the cold cavity resonance frequency of the mode (q,n). We also assume that these modes are orthogonal for the same frequency component q:

$$\iiint_{\text{cavity}} u_{q,n}(\mathbf{r})u_{q,n}^*(\mathbf{r})dxdydz = V_{q,n}, \tag{2.10}$$

$$\iiint_{\text{cavity}} u_{q,n}(\mathbf{r})u_{q,n'}^*(\mathbf{r})dxdydz = 0 \quad (n \neq n'), \tag{2.11}$$

where $V_{q,n}$ is the mode volume occupied by the q-th frequency component in the n-th spatial mode. In the cw Raman laser systems we will study later, all the intracavity fields (q = pump, Stokes, anti-Stokes...) will be in single spatial modes. Therefore we can drop the subscript n in the equations (2.8) through (2.10) and Eq.(2.8) can be written as

$$E_q(\mathbf{r},t) = E_q(t)u_q(\mathbf{r}). \tag{2.12}$$

Next we substitute Eq.(2.12) and the Laplace equation (2.9) into Eq. (2.6), multiply $u_q^*(z)$ and perform the volume integral (normalized by the volume V_q)

$$\frac{1}{V_q}\iiint_{\text{cavity}} dxdydz \doteq \frac{1}{V_q}\int_{-L/2}^{L/2} dz \int_0^{\infty} rdr \int_0^{2\pi} d\phi \tag{2.13}$$

on both sides. By using Eq.(2.10), we obtain for each frequency component q,

$$\dot{E}_q(t) + \left[\frac{\gamma_{cq}}{2} - i(\omega_q - \omega_{cq})\right] E_q(t) = i\frac{\omega_q}{2\epsilon_0} P_q(t) + \frac{\gamma_{eq}}{2} E_{eq}(t), \tag{2.14}$$

where $P_q(t)$ is given by:

$$P_q(t) = \frac{1}{V_q}\iiint_{\text{cavity}} dxdydz P_q(\mathbf{r},t) u_q^*(\mathbf{r}). \tag{2.15}$$

In deriving Eq.(2.14), $\omega_q^2 - \omega_{cq}^2 \approx 2\omega_q(\omega_q - \omega_{cq})$ has been used.

In order to solve the field equation (2.14), we need to know the relation between P and E.. So in the next section we develop the density-matrix equations.

Density Matrix Equations

Theoretical model and Schrödinger equation

We consider a far-off-resonance multilevel Λ-configuration system as shown in Fig. 2.

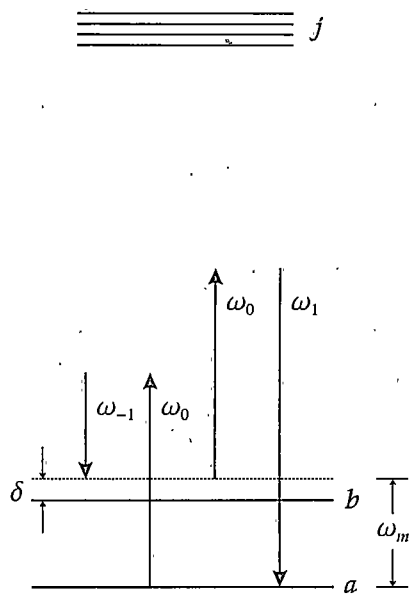

Figure 2 Energy levels and laser fields for the far-off-resonance Raman process. The lowest level a is the ground state and the higher level b can be either a vibrational state or a rotational state. We allow an arbitrary number of higher level j and all possible orders of Stokes and anti-Stokes [labeled by an integer q and here only shows $q = \pm 1$ ($q = 0$ is the pump)] generated by the Raman process for the most generality. The transition between levels a and b is electric dipole forbidden. The transitions $j \leftrightarrow a$ and $j \leftrightarrow b$ are far off single-photon resonances and there may be a two-photon detuning δ for the $a \leftrightarrow b$ transition ($\delta < 0$ in the configuration shown).

There are multiple upper levels j and two lower levels a and b, as well as multiple laser fields with frequencies ω_q (q = integer). Levels j (with energies ω_j) are coupled to the two lower levels (with energies ω_a and ω_b) by electric dipole transitions, while the transition between a and b is electric dipole forbidden. The transitions $j \leftrightarrow a$ and $j \leftrightarrow b$ are far off single-photon resonances and there may be a two-photon detuning δ for the $a \leftrightarrow b$ transition. The results of this model have been given by Harris [26, 27] and Fam Le Kien [28]. In this section, we derive it in detail.

The multiple fields are given by Eq. (2.2)[2]:

$$\tilde{E} = \frac{1}{2}\sum_q (E_q e^{-i\omega_q t} + \text{c.c.}), \tag{2.16}$$

where

$$\omega_q = \omega_0 + q(\omega_b - \omega_a - \delta) = \omega_0 + q\omega_m, \tag{2.17}$$

or

$$\omega_q = \omega_{q-1} + q\omega_m. \tag{2.18}$$

In the cw Raman laser, we have only two fields: $q = 0$ for the pump and $q = -1$ for the first-order Stokes. But we still do our derivation for multiple fields so that the density matrix equations can be easily extended to other cases, for example, the anti-Stokes emission.

The system Hamiltonian can be written as this matrix form:

$$H = \begin{pmatrix} \hbar\omega_a & 0 & \cdots & V_{aj} & \cdots \\ 0 & \hbar\omega_b & \cdots & V_{bj} & \cdots \\ \vdots & \vdots & \ddots & \vdots & \\ V_{ja} & V_{jb} & \cdots & \hbar\omega_j & \cdots \\ \vdots & \vdots & & \vdots & \ddots \end{pmatrix}, \tag{2.19}$$

where

$$V_{aj} = V_{ja}^* = -\mu_{aj} \cdot \frac{1}{2}\sum_q (E_q e^{-i\omega_q t} + \text{c.c.}), \tag{2.20a}$$

$$V_{bj} = V_{jb}^* = -\mu_{bj} \cdot \frac{1}{2}\sum_q (E_q e^{-i\omega_q t} + \text{c.c.}), \tag{2.20b}$$

and μ_{aj} and μ_{bj} are the dipole moments between levels $a \leftrightarrow j$ and $b \leftrightarrow j$ respectively.

[2] If written in full notation, $\tilde{E} = \tilde{E}(\mathbf{r}, t)$ and $E_q = E_q(\mathbf{r}, t)$, but here we take the shorter notation because all the fields will be functions of $\mathbf{r}$ and t throughout this section.

The wavefunction of the system is

$$|\psi(t)\rangle = \sum_n C'_n e^{-i\omega_n t}|n\rangle, \tag{2.21}$$

where $n = a, b, j$. The amplitude C'_n obeys the Schrödinger equation:

$$i\hbar \dot{C}'_n = \sum_k e^{-i\omega_{nk}t} V_{nk} C'_k, \tag{2.22}$$

where $\omega_{nk} = \omega_n - \omega_k$. By making the transformation

$$C_a = C'_a, \qquad C_b = C'_b e^{-i\delta t}, \qquad C_j = C'_j, \tag{2.23}$$

Eq. (2.22) becomes

$$\dot{C}_a = \frac{i}{2\hbar} \sum_j C_j \mu_{aj} \left[\sum_q E_q e^{-i(\omega_{ja}+\omega_q)t} + \sum_q E_q^* e^{-i(\omega_{ja}-\omega_q)t} \right], \tag{2.24a}$$

$$\dot{C}_b = -i\delta C_b + \frac{i}{2\hbar} \sum_j C_j \mu_{bj} \left[\sum_q E_q e^{-i(\omega_{jb}+\omega_q)t} + \sum_q E_q^* e^{-i(\omega_{jb}-\omega_q)t} \right], \tag{2.24b}$$

$$\begin{aligned} \dot{C}_j = {} & \frac{i}{2\hbar} C_a \mu_{ja} \left[\sum_q E_q e^{i(\omega_{ja}-\omega_q)t} + \sum_q E_q^* e^{i(\omega_{ja}+\omega_q)t} \right] \\ & + \frac{i}{2\hbar} C_b \mu_{jb} \left[\sum_q E_q e^{i(\omega_{jb}-\omega_q)t} + \sum_q E_q^* e^{i(\omega_{jb}+\omega_q)t} \right], \end{aligned} \tag{2.24c}$$

Since $\omega_{jb} \pm \omega_q + \delta = \omega_{ja} \pm \omega_{q\mp 1}$, Eqs. (2.24) can be written in terms of ω_{ja} only:

$$\dot{C}_a = \frac{i}{2\hbar} \sum_j C_j \mu_{aj} \left[\sum_q E_q e^{-i(\omega_{ja}+\omega_q)t} + \sum_q E_q^* e^{-i(\omega_{ja}-\omega_q)t} \right], \tag{2.25a}$$

$$\dot{C}_b = -i\delta C_b + \frac{i}{2\hbar} \sum_j C_j \mu_{bj} \left[\sum_q E_{q+1} e^{-i(\omega_{ja}+\omega_q)t} + \sum_q E_{q-1}^* e^{-i(\omega_{ja}-\omega_q)t} \right], \tag{2.25b}$$

$$\dot{C}_j = \frac{i}{2\hbar} C_a \mu_{ja} \left[\sum_q E_q e^{i(\omega_{ja}-\omega_q)t} + \sum_q E_q^* e^{i(\omega_{ja}+\omega_q)t} \right]$$
$$+ \frac{i}{2\hbar} C_b \mu_{jb} \left[\sum_q E_{q-1} e^{i(\omega_{ja}-\omega_q)t} + \sum_q E_{q+1}^* e^{i(\omega_{ja}+\omega_q)t} \right], \qquad (2.25c)$$

Adiabatic elimination of C_j

Because of the far-off-resonance condition, we assume that for all times the upper levels j are in steady state. Therefore in the Schrödinger equation (2.25), we perform adiabatic elimination of C_j by first integrating Eq. (2.25c):

$$C_j = \frac{i}{2\hbar} \int_{-\infty}^{t} \left[\sum_q e^{i(\omega_{ja}-\omega_q)t'} (C_a \mu_{ja} E_q + C_b \mu_{jb} E_{q-1}) \right] dt'$$
$$+ \frac{i}{2\hbar} \int_{-\infty}^{t} \left[\sum_q e^{i(\omega_{ja}+\omega_q)t'} (C_a \mu_{ja} E_q^* + C_b \mu_{jb} E_{q+1}^*) \right] dt'.$$

Compared with $e^{i(\omega_{ja}\pm\omega_q)t}$, C_a, C_b and E_q vary slowly in time so they can be taken out of the integral:

$$C_j = \frac{1}{2\hbar} \sum_q \frac{e^{i(\omega_{ja}-\omega_q)t}}{\omega_{ja}-\omega_q} (C_a \mu_{ja} E_q + C_b \mu_{jb} E_{q-1})$$
$$+ \frac{1}{2\hbar} \sum_q \frac{e^{i(\omega_{ja}+\omega_q)t}}{\omega_{ja}+\omega_q} (C_a \mu_{ja} E_q^* + C_b \mu_{jb} E_{q+1}^*). \qquad (2.26)$$

Substituting C_j into Eq. (2.25a) and (2.25b) and dropping all the fast oscillating terms (slowly-varying amplitude approximation), we get

$$\dot{C}_a = \frac{i}{(2\hbar)^2} C_a \sum_q \sum_j |\mu_{aj}|^2 |E_q|^2 \left(\frac{1}{\omega_{ja}-\omega_q} + \frac{1}{\omega_{ja}+\omega_q} \right)$$
$$+ \frac{i}{(2\hbar)^2} C_b \sum_q \sum_j \mu_{aj} \mu_{jb} E_q E_{q+1}^* \left(\frac{1}{\omega_{jb}-\omega_q} + \frac{1}{\omega_{ja}+\omega_q} \right), \qquad (2.27a)$$

$$\dot{C}_b = -i\delta C_b + \frac{i}{(2\hbar)^2} C_a \sum_q \sum_j \mu_{bj}\mu_{ja} E_q E_{q+1}^* \left(\frac{1}{\omega_{jb} - \omega_q} + \frac{1}{\omega_{ja} + \omega_q} \right)$$
$$+ \frac{i}{(2\hbar)^2} C_b \sum_q \sum_j |\mu_{bj}|^2 |E_q|^2 \left(\frac{1}{\omega_{jb} - \omega_q} + \frac{1}{\omega_{jb} + \omega_q} \right), \quad (2.27b)$$

where we have used

$$\omega_{ja} - \omega_q = \omega_{jb} - \omega_{q-1} + \delta \approx \omega_{jb} - \omega_{q-1},$$
$$\omega_{ja} + \omega_q = \omega_{jb} + \omega_{q+1} + \delta \approx \omega_{jb} + \omega_{q+1}. \quad (2.28)$$

Eqs. (2.27) can be written as a simple form

$$\frac{d}{dt} \begin{pmatrix} C_a \\ C_b \end{pmatrix} = i \begin{pmatrix} \Omega_{aa} & \Omega_{ab} \\ \Omega_{ab}^* & \Omega_{bb} - \delta \end{pmatrix} \begin{pmatrix} C_a \\ C_b \end{pmatrix}, \quad (2.29)$$

where we have introduced the Stark shifts

$$\Omega_{aa} = \frac{1}{2} \sum_q a_q |E_q|^2, \quad (2.30a)$$
$$\Omega_{bb} = \frac{1}{2} \sum_q b_q |E_q|^2, \quad (2.30b)$$

and the two-photon Rabi frequency

$$\Omega_{ab} = \frac{1}{2} \sum_q d_q E_q E_{q+1}^*. \quad (2.31)$$

The constants a_q, b_q and d_q, with units of $[\mathrm{m}^2 \cdot \mathrm{V}^{-2} \cdot \mathrm{s}^{-1}]$, are related to the dipole moments and the single-photon detunings:

$$a_q = \frac{1}{2\hbar^2} \sum_j |\mu_{aj}|^2 \left(\frac{1}{\omega_{ja} - \omega_q} + \frac{1}{\omega_{ja} + \omega_q} \right), \quad (2.32a)$$
$$b_q = \frac{1}{2\hbar^2} \sum_j |\mu_{bj}|^2 \left(\frac{1}{\omega_{jb} - \omega_q} + \frac{1}{\omega_{jb} + \omega_q} \right), \quad (2.32b)$$
$$d_q = \frac{1}{2\hbar^2} \sum_j \mu_{aj}\mu_{jb} \left(\frac{1}{\omega_{jb} - \omega_q} + \frac{1}{\omega_{ja} + \omega_q} \right). \quad (2.32c)$$

Density-matrix equations

The density-matrix equations can be obtained from Eq. (2.29). The density-matrix elements are defined by:

$$\tilde{\rho}_{ab} = C'_a e^{-i\omega_a t} \cdot C'^*_b e^{i\omega_b t} = C_a C^*_b e^{i\omega_m t} = \rho_{ab} e^{i\omega_m t}, \tag{2.33a}$$

$$\tilde{\rho}_{aa} = |C_a|^2 = \rho_{aa}, \tag{2.33b}$$

$$\tilde{\rho}_{bb} = |C_b|^2 = \rho_{bb}. \tag{2.33c}$$

Then from Eq. (2.29),

$$\dot{\rho}_{aa} = i(\Omega_{ab}\rho_{ba} - \Omega_{ba}\rho_{ab}) + \Gamma_{ba}\rho_{bb}, \tag{2.34a}$$

$$\dot{\rho}_{bb} = -i(\Omega_{ab}\rho_{ba} - \Omega_{ba}\rho_{ab}) - \Gamma_{ba}\rho_{bb}, \tag{2.34b}$$

$$\dot{\rho}_{ab} = i(\Omega_{aa} - \Omega_{bb} + \delta)\rho_{ab} + i\Omega_{ab}(\rho_{bb} - \rho_{aa}) - \gamma_{ab}\rho_{ab}, \tag{2.34c}$$

where the phenomenological damping has been included: Γ_{ba} is a population decay rate from level b to a and γ_{ab} is a coherence dephasing rate. They both have the units of radians per second[3].

We note that if we change the two-photon Rabi frequency to a single-photon Rabi frequency and ignore the relative Stark shift $\Omega_{aa} - \Omega_{bb}$, then Eqs. (2.34) are simply the density-matrix equations for a two-level atom in the presence of one optical field [13, page 200], where δ becomes the single-photon-detuning. In other words, the

[3] Note that in this chapter, all the quantities associated with frequency or rate are with angular frequency. For example, these quantities: ω_{ja}, Ω_{ab}, δ, and γ_{ab}, etc., all have the units of rad/sec.

adiabatic elimination of the upper levels j simplifies our system to an effective two-level problem.

The polarization

The polarization density $\tilde{P} = \tilde{P}(\mathbf{r}, t)$ in Eq.(2.3) is defined by

$$\tilde{P} = N\mathrm{tr}(\tilde{\rho}\mu) = N\sum_j \left(\mu_{ja}\tilde{\rho}_{aj} + \mu_{aj}\tilde{\rho}_{ja} + \mu_{jb}\tilde{\rho}_{bj} + \mu_{bj}\tilde{\rho}_{jb}\right), \tag{2.35}$$

where N is the atomic density and the density matrix elements $\tilde{\rho}_{aj}$ and $\tilde{\rho}_{bj}$ are defined by, similar to Eq. (2.33a),

$$\tilde{\rho}_{aj} = C'_a e^{-i\omega_a t} \cdot C'^*_j e^{i\omega_j t} = C_a C^*_j e^{-i\omega_{aj} t}, \tag{2.36}$$

$$\tilde{\rho}_{bj} = C'_b e^{-i\omega_b t} \cdot C'^*_j e^{i\omega_j t} = C_b C^*_j e^{-i(\omega_{bj} - \delta)t}. \tag{2.37}$$

By substituting Eq. (2.26) into Eq. (2.35) and using Eq. (2.28) we find in the expansion Eq.(2.3),

$$P_q(\mathbf{r}, t) = 2N\hbar(a_q\rho_{aa}E_q + b_q\rho_{bb}E_q + d_{q-1}\rho_{ba}E_{q-1} + d^*_q\rho_{ab}E_{q+1}). \tag{2.38}$$

With Eqs. (2.14), (2.34), and (2.38), we are now ready to solve for the far-off-resonance intracavity Raman process.

The Stokes Laser

In this section, as illustrated in Fig. 3, we consider only two fields: $q = 0$ for the pump and $q = -1$ for the first-order Stokes. We use the subscripts p and s to denote the "pump" and the "Stokes" respectively.

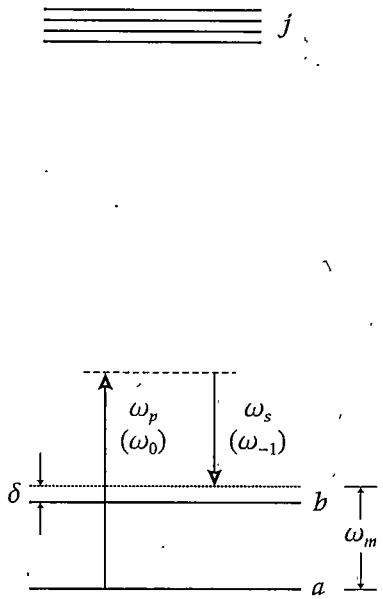

Figure 3 Energy levels and laser fields for the Stokes laser. Level a is the ground state; level b can be either a vibrational state or a rotational state; levels denoted by j are multiple excited electronic states. The pump field ω_p $(q = 0)$ is red-shifted to the Stokes field ω_s $(q = -1)$ and a molecular coherence $\rho_{ab}e^{i\omega_m t}$ is established between levels a and b. There can be a two-photon detuning denoted by δ.

Population and coherence

Because of the far-off-resonance condition, we can neglect the population on the upper levels j [4]. Therefore we assume

$$\rho_{aa} + \rho_{bb} = 1. \tag{2.39}$$

Define $D = \rho_{bb} - \rho_{aa}$ to be the population difference between levels b and a. By using

[4] Specifically, this is due to $\Omega \ll \Delta$ in our system, where $\Omega \sim 10^{10}$ rad/sec is the single-photon Rabi frequency of either the pump or the Stokes field and $\Delta \sim 10^{16}$ rad/sec is the single-photon detuning. This can be understood by solving the "two-level atom with one field" problem, which is given in many quantum optics textbooks. See, for example, Boyd [13], Eq.(5.3.11), when $\Omega \ll \Delta$ is satisfied, almost no population can be excited to the upper level.

Eq. (2.39), the density matrix equations (2.34) can be written as

$$\dot{D} = -2i(\Omega_{ab}\rho_{ba} - \Omega_{ba}\rho_{ab}) - \Gamma_{ba}(D - D^{eq}), \tag{2.40a}$$

$$\dot{\rho}_{ab} = -\big[\gamma_{ab} - i(\Omega_{aa} - \Omega_{bb} + \delta)\big]\rho_{ab} + i\Omega_{ab}D, \tag{2.40b}$$

where the Stark shifts Ω_{aa} and Ω_{bb} have been given by Eq. (2.30):

$$\Omega_{aa} = \frac{1}{2}\big(a_p|E_p|^2 + a_s|E_s|^2\big), \tag{2.41a}$$

$$\Omega_{bb} = \frac{1}{2}\big(b_p|E_p|^2 + b_s|E_s|^2\big), \tag{2.41b}$$

and the two-photon Rabi frequency [given by Eq. (2.31)]

$$\Omega_{ab} = \frac{d_s}{2}E_s(\mathbf{r},t)E_p^*(\mathbf{r},t) \tag{2.42}$$

contains the pump and Stokes fields which drive the coherence ρ_{ab}. The dispersion constants $a_{p(s)}$ and $b_{p(s)}$ are defined by Eqs. (2.32a) and (2.32b):

$$a_{p(s)} = \frac{1}{2\hbar^2}\sum_j |\mu_{aj}|^2 \left(\frac{1}{\omega_{ja} - \omega_{p(s)}} + \frac{1}{\omega_{ja} + \omega_{p(s)}}\right), \tag{2.43a}$$

$$b_{p(s)} = \frac{1}{2\hbar^2}\sum_j |\mu_{bj}|^2 \left(\frac{1}{\omega_{jb} - \omega_{p(s)}} + \frac{1}{\omega_{jb} + \omega_{p(s)}}\right). \tag{2.43b}$$

The coupling constant d_s is defined by Eq. (2.32c):

$$d_s = \frac{1}{2\hbar^2}\sum_j \mu_{aj}\mu_{jb} \left(\frac{1}{\omega_{jb} - \omega_s} + \frac{1}{\omega_{ja} + \omega_s}\right). \tag{2.44}$$

We will take d_s to be a real number for simplicity. In Eq. (2.40a), we have included a population difference in thermal equilibrium denoted by D^{eq} [13, Page 196] and we assume $D^{eq} = -1$, i.e., all the population is in the ground state in thermal equilibrium.

At steady state, all the time derivatives are set to zero. Eqs. (2.40) can then be solved algebraically:

$$D = \frac{\Gamma_{ba} D^{eq} (\gamma_{ab}^2 + \delta^2)}{\Gamma_{ba} (\gamma_{ab}^2 + \delta^2) + 4|\Omega_{ab}|^2 \gamma_{ab}}, \tag{2.45a}$$

$$\rho_{ab} = \frac{i\Omega_{ab} D}{\gamma_{ab} - i(\Omega_{aa} - \Omega_{bb} + \delta)}. \tag{2.45b}$$

We can estimate steady-state values of the population difference D and the coherence amplitude $|\rho_{ab}|$ in the cw Raman lasers. At room temperature, for the pure vibrational $v = 0 \rightarrow 1$ transition in 10 atm H_2, the population decay rate $\Gamma_{ba} \approx 2\pi \times 1 \times 10^4$ rad/s [29] and the Raman gain linewidth (HWHM) $\gamma_{ab} \approx 2\pi \times 250 \times 10^6$ rad/s [3]. The constants $a_{p(s)}$, $b_{p(s)}$, and d_s have been calculated by Fam Le Kien et al [28]: $a_p \approx a_s \approx 2.6 \times 10^{-7}$, $b_p \approx b_s \approx 2.8 \times 10^{-7}$, and $d_s \approx 6.1 \times 10^{-8}$, in the SI units (i.e., $\mathrm{m}^2 \cdot \mathrm{V}^{-2} \cdot \mathrm{s}^{-1}$). If we assume that the input pump power is 10 mW and both the cavity mirrors have a reflectance of 0.9999, then the intracavity spatial peak pump power is approximately 28 W. Converting this intracavity power to field amplitude and assuming the Stokes field has the same intracavity amplitude, we calculate that the Stark shifts $\Omega_{aa} \approx 1.0 \times 10^5$ rad/s, $\Omega_{bb} \approx 1.1 \times 10^5$ rad/s, and the two-photon Rabi frequency $\Omega_{ab} \approx 1.2 \times 10^4$ rad/s. Using all these data, we obtain that for the vibrational Raman laser and at the gain line center ($\delta = 0$),

$$D \approx -0.99996, \tag{2.46a}$$

$$|\rho_{ab}| \approx 8 \times 10^{-6}. \tag{2.46b}$$

This calculation shows that, because of $\Gamma_{ba}\gamma_{ab} \gg \Omega_{ab}^2$, the population for the cw

Raman laser can be considered undepleted from the ground state a (or $D \approx D^{eq}$) and therefore we can ignore the population equation (2.40a) for the later theoretical work. This calculation also tells us that, because of $\gamma_{ab} \gg \Omega_{ab}$, the coherence ρ_{ab} has a very small amplitude, far from the region of electromagnetically induced transparency [30], in which the coherence can be built up to its maximum value of 0.5 [26].

Polarization and Raman gain

In the two-field condition, Eq.(2.38) now becomes

$$P_p(\mathbf{r},t) = 2N\hbar\big[(a_p\rho_{aa} + b_p\rho_{bb})E_p(\mathbf{r},t) + d_s\rho_{ba}(\mathbf{r},t)E_s(\mathbf{r},t)\big], \tag{2.47a}$$

$$P_s(\mathbf{r},t) = 2N\hbar\big[(a_s\rho_{aa} + b_s\rho_{bb})E_s(\mathbf{r},t) + d_s\rho_{ab}(\mathbf{r},t)E_p(\mathbf{r},t)\big], \tag{2.47b}$$

where, as given by Eq.(2.12),

$$E_{p(s)}(\mathbf{r},t) = E_{p(s)}(t)u_{p(s)}(\mathbf{r}). \tag{2.48}$$

Before we derive the intracavity field equations, let's first connect ρ_{ab} to some real physical quantities. Substituting (2.45b) into (2.47b), we obtain

$$P_s = 2N\hbar(a_s\rho_{aa} + b_s\rho_{bb})E_s + i\frac{N\hbar d_s^2 D}{\gamma_{ab} - i(\Omega_{aa} - \Omega_{bb} + \delta)}|E_p|^2E_s. \tag{2.49}$$

Since $\rho_{aa} \approx 1$ and $\rho_{bb} \approx 0$, and $\Omega_{aa} \approx \Omega_{bb}$ (i.e., we ignore the population on level b and the relative Stark shift $\Omega_{aa} - \Omega_{bb}$), the Stokes polarization has the form

$$P_s = 2N\hbar a_s E_s + i\frac{N\hbar d_s^2 D}{\gamma_{ab} - i\delta}|E_p|^2E_s. \tag{2.50}$$

Comparing with the definition [31, Page 471]

$$P_s = \epsilon_0\chi^{(1)}E_s - \epsilon_0\chi^{(3)}|E_p|^2E_s, \tag{2.51}$$

where $\chi^{(1)}$, the linear susceptibility, is associated with the refractive index change caused by the single-photon-induced dispersion in the medium by the form

$$n_s = \sqrt{1+\chi^{(1)}} \approx 1 + \frac{\chi^{(1)}}{2}, \tag{2.52}$$

we obtain

$$n_s \approx 1 + N\hbar a_s/\epsilon_0. \tag{2.53}$$

The $\chi^{(3)}$ in the second term of Eq. (2.51) is the complex Raman nonlinear susceptibility. It can be split into real and imaginary parts in the form $\chi'_R - i\chi''_R$, where

$$\chi'_R = -\frac{N\hbar d_s^2 D\delta}{\epsilon_0\left(\gamma_{ab}^2+\delta^2\right)}, \tag{2.54a}$$

$$\chi''_R = -\frac{N\hbar d_s^2 D\gamma_{ab}}{\epsilon_0\left(\gamma_{ab}^2+\delta^2\right)}. \tag{2.54b}$$

To see the physical roles of χ'_R and χ''_R, we note from Eq. (2.14) that the Stokes field is driven by a term proportional to iP_s. Therefore the two-photon (Raman) induced dispersion is reflected by the real part χ'_R; while the Raman plane-wave gain coefficient[5] is proportional to the imaginary part of the Raman susceptibility [32, 33]:

$$\alpha_g = \frac{2\omega_s\chi''_R}{n_s n_p c^2\epsilon_0} = \frac{2\omega_s N\hbar d_s^2(-D)\gamma_{ab}}{n_s n_p c^2\epsilon_0^2(\gamma_{ab}^2+\delta^2)}. \tag{2.55}$$

---

[5] For the case of SRS in free space, using the classical wave equation, one should obtain that the Stokes field experiences spatially exponential growth in the form [32]

$$\frac{\partial E_s}{\partial z} = \frac{\omega_s}{2cn_s}\chi''_R|E_p|^2E_s = \frac{g_s}{2}E_s,$$

where g_s is the Stokes power gain. When the pump beam is a plane wave with uniform transverse intensity, the Stokes power gain per unit pump intensity g_s/I_s is defined as the plane-wave gain coefficient.

By substituting Eq.(2.45a), we can write α_g in the following form:

$$\alpha_g(\delta) = \alpha_g(0)\left(1+\frac{4|\Omega_{ab}|^2}{\gamma_{ab}\Gamma_{ba}}\right)^{-1}\left(1+\frac{\delta^2}{\gamma_{ab}^2}\frac{1}{1+4|\Omega_{ab}|^2/\gamma_{ab}\Gamma_{ba}}\right)^{-1}, \tag{2.56}$$

where

$$\alpha_g(0) = \frac{2\omega_s N\hbar d_s^2(-D^{eq})}{n_s n_p c^2\epsilon_0^2\gamma_{ab}} \tag{2.57}$$

is the line center value of the unsaturated or small-signal plane-wave gain coefficient. This value is decreased by the factor $(1+4|\Omega_{ab}|^2/\gamma_{ab}\Gamma_{ba})^{-1}$, a phenomenon called saturation [13, page 203]. The last term in Eq. (2.56) indicates that the Raman gain has a Lorentzian lineshape with a FWHM linewidth of $2\gamma_{ab}\cdot\sqrt{1+4|\Omega_{ab}|^2/\gamma_{ab}\Gamma_{ba}}$. The small-signal linewidth $2\gamma_{ab}$ is broadened by the factor $\sqrt{1+4|\Omega_{ab}|^2/\gamma_{ab}\Gamma_{ba}}$, an effect called power broadening [13, page 202].

We can calculate the Raman plane-wave gain coefficient $\alpha_g(0)$ using Eq.(2.57). At a pressure of 10 atm and a temperature of 300 K, the hydrogen number density $N = 2.432\times10^{26}\ \mathrm{m}^{-3}$ [1, page 4-118]; for the pure vibrational $v=0\rightarrow1$ transition, the Raman gain linewidth (HWHM) $\gamma_{ab} = 2\pi\times250\times10^6$ rad/s [3]; the coupling constant $d_s \approx 6.1\times10^{-8}\ \mathrm{m^2Hz/V^2}$ [28]. By taking $n_s\approx n_p\approx1$, $D^{eq}\approx-1$ and the Stokes wavelength of 1180 nm, we get $\alpha_{gv}(0) = 1.4\times10^{-11}$ m/W. Experimentally measured value of the Raman plane-wave gain coefficient for the vibrational transition pumped at 792 nm is $\alpha_{gv}(0) = 1.5\times10^{-11}$ m/W [2]. Our theoretical calculation is very close to this value.

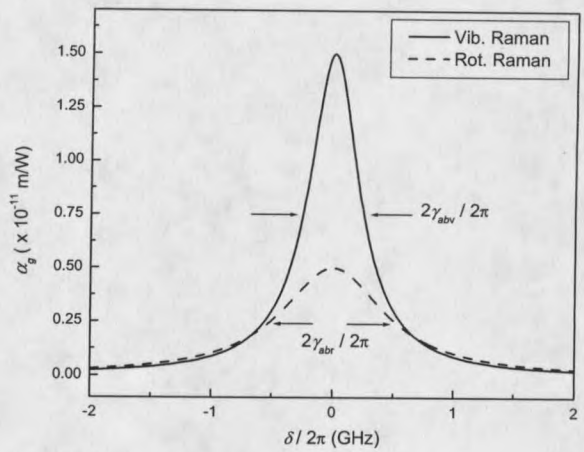

Figure 4 Raman plane-wave gain coefficient as a function of the two photon detuning. For the vibrational Raman transition (792→1180 nm, solid line), $\alpha_{gv}(0) = 1.5 \times 10^{-11}$ m/W [2], linewidth (HWHM) $\gamma_{abv}/2\pi = 250$ MHz [3]. For the rotational transition (792→830 nm, dashed line), $\alpha_{gr}(0) = 0.5 \times 10^{-11}$ m/W [4, 5, 6], linewidth (HWHM) $\gamma_{abr}/2\pi = 510$ MHz [7]. Gain and linewidth are for 10 atm H_2 at 300 K room temperature.

The gain saturation and linewidth broadening shown by Eq. (2.56) can also be estimated: the population decay rate $\Gamma_{ba}/2\pi$ is approximately 10 kHz [29]; the typical intracavity power of both the pump and Stokes is around 10 W. Then it can be calculated that the gain saturation factor is about 0.999997 and the linewidth broadening factor is about 1.000003. Both effects are small and thus negligible.

Intracavity field equations

Now we are ready to derive the intracavity field equations for the Stokes laser. We assume that the coherence establishes its steady-state value much faster than the intracavity fields (adiabatic following approximation [13, page 212]). Then the steady-state solution of ρ_{ab}, i.e., Eq.(2.45b), can be used for the field equations. We first obtain the polarization amplitudes at the pump and Stokes frequencies by

substituting Eq.(2.45b) to Eqs.(2.47):

$$P_p(\mathbf{r},t) = 2N\hbar a_p E_p(t)u_p(\mathbf{r}) - i\frac{N\hbar d_s^2 D}{\gamma_{ab}+i\delta}|E_s(t)u_s(\mathbf{r})|^2 E_p(t)u_p(\mathbf{r}), \tag{2.58a}$$

$$P_s(\mathbf{r},t) = 2N\hbar a_s E_s(t)u_s(\mathbf{r}) + i\frac{N\hbar d_s^2 D}{\gamma_{ab}-i\delta}|E_p(t)u_p(\mathbf{r})|^2 E_s(t)u_s(\mathbf{r}), \tag{2.58b}$$

where we have ignored the population on level b (i.e., $\rho_{aa} \approx 1$ and $\rho_{bb} \approx 0$, or $D \approx -1$) as well as the relative Stark shift (i.e., $\Omega_{aa} - \Omega_{bb} \approx 0$). The continuous-wave Raman laser is a double-resonance laser system, i.e., both the pump and Stokes fields are resonant with the cavity. Thus both fields should observe the intracavity field equation (2.14), or

$$\dot{E}_p(t) + \left[\frac{\gamma_{cp}}{2} - i(\omega_p - \omega_{cp})\right] E_p(t) = \frac{\gamma_{ep}}{2}E_{ep}(t) + i\frac{\omega_p}{2\epsilon_0}\frac{1}{V_p}\iiint_{\text{cavity}} dxdydz P_p(\mathbf{r},t)u_p^*(\mathbf{r}), \tag{2.59a}$$

$$\dot{E}_s(t) + \left[\frac{\gamma_{cs}}{2} - i(\omega_s - \omega_{cs})\right] E_s(t) = i\frac{\omega_s}{2\epsilon_0}\frac{1}{V_s}\iiint_{\text{cavity}} dxdydz P_s(\mathbf{r},t)u_s^*(\mathbf{r}). \tag{2.59b}$$

Substituting Eqs.(2.58) into (2.59), we obtain

$$\dot{E}_p(t) + \left[\frac{\gamma_{cp}}{2} - i\left(\omega_p - \omega_{cp}\right)\right] E_p(t) = i\omega_p\frac{N\hbar a_p}{\epsilon_0}\frac{V_p}{V_p}E_p(t) + \omega_p\frac{N\hbar d_s^2 D}{2\epsilon_0}\frac{1}{\gamma_{ab}+i\delta}\frac{V_{ps}}{V_p}|E_s(t)|^2 E_p(t) + \frac{\gamma_{ep}}{2}E_{ep}(t), \tag{2.60a}$$

$$\dot{E}_s(t) + \left[\frac{\gamma_{cs}}{2} - i\left(\omega_s - \omega_{cs}\right)\right] E_s(t) = i\omega_s\frac{N\hbar a_s}{\epsilon_0}\frac{V_s}{V_s}E_s(t) - \omega_s\frac{N\hbar d_s^2 D}{2\epsilon_0}\frac{1}{\gamma_{ab}-i\delta}\frac{V_{ps}}{V_s}|E_p(t)|^2 E_s(t), \tag{2.60b}$$

where the cavity's single mode-volumes V_p and V_s and the two-field overlap mode-volume V_{ps} are given by

$$V_{p(s)} = \int_{-L/2}^{L/2} dz \int_0^\infty r dr \int_0^{2\pi} d\phi |u_{p(s)}|^2, \tag{2.61a}$$

$$V_{ps} = \int_{-L/2}^{L/2} dz \int_0^{\infty} r dr \int_0^{2\pi} d\phi |u_p|^2 |u_s|^2. \tag{2.61b}$$

In a stable two-mirror laser cavity of length L and in the TEM_{00} spatial mode, $u_q(\mathbf{r})$ is of the form [32]

$$u_q(\mathbf{r}) = u_q(r,z) = \frac{1}{1+i2z/b_q} e^{-r^2 k_q / b_q (1+i2z/b_q)} \sin(k_q z), \tag{2.62}$$

where $r^2 = x^2 + y^2$. Here k_q and b_q are the wave vector and the confocal parameter (twice the Rayleigh range) of the q-th field respectively.

With Eq.(2.62), noting that the confocal parameter b is the same for both the pump and the Stokes since it is only determined by the cavity's geometric property, we compute the above integrals to obtain

$$V_{p(s)} = 2\pi \frac{L}{8} \frac{b}{k_{p(s)}}, \tag{2.63a}$$

$$V_{ps} = 2\pi \frac{1}{16} \frac{b^2}{k_p + k_s} \tan^{-1}\left(\frac{L}{b}\right). \tag{2.63b}$$

Then Eqs.(2.60) become

$$\dot{E}_p(t) + \left\{ \frac{\gamma_{cp}}{2} - i \left[\left(\frac{N\hbar a_p}{\epsilon_0} + 1 \right) \omega_p - \omega_{cp} \right] \right\} E_p(t) = \frac{\gamma_{ep}}{2} E_{ep}(t) + \frac{1}{4} \omega_p \frac{N\hbar d_s^2 D}{\epsilon_0} \frac{1}{\gamma_{ab} + i\delta} \frac{\lambda_s}{\lambda_p + \lambda_s} \frac{\tan^{-1}(L/b)}{L/b} |E_s(t)|^2 E_p(t), \tag{2.64a}$$

$$\dot{E}_s(t) + \left\{ \frac{\gamma_{cs}}{2} - i \left[\left(\frac{N\hbar a_s}{\epsilon_0} + 1 \right) \omega_s - \omega_{cs} \right] \right\} \dot{E}_s(t) = -\frac{1}{4} \omega_s \frac{N\hbar d_s^2 D}{\epsilon_0} \frac{1}{\gamma_{ab} - i\delta} \frac{\lambda_p}{\lambda_p + \lambda_s} \frac{\tan^{-1}(L/b)}{L/b} |E_p(t)|^2 E_s(t). \tag{2.64b}$$

We can define a gain term

$$G(\delta) = -\frac{1}{4}\omega_s \frac{N\hbar d_s^2 D}{\epsilon_0} \frac{\gamma_{ab}}{\gamma_{ab}^2+\delta^2} \frac{\lambda_p}{\lambda_p+\lambda_s} \frac{\tan^{-1}(L/b)}{L/b}$$
$$= \frac{1}{8} c^2 \epsilon_0 \alpha_g(\delta) \frac{\lambda_p}{\lambda_p+\lambda_s} \frac{\tan^{-1}(L/b)}{L/b}, \tag{2.65}$$

where $\alpha_g(\delta)$ is the plane-wave gain coefficient given by Eq.(2.55). Eq.(2.65) has the same form as the gain defined by Brasseur[21, Eq.(3)] if

$$\frac{\tan^{-1}(L/b)}{L/b} \approx 1. \tag{2.66}$$

This relation is valid if the laser cavity's length is well within the confocal parameter (or twice the Rayleigh range) of the laser beam, so that the beam inside the cavity can be considered collimated. This is true for all the cw Raman lasers that have been demonstrated so far.

Eqs. (2.64) now has the form

$$\dot{E}_p(t) + \left[\frac{\gamma_{cp}}{2} - i(n_p\omega_p - \omega_{cp})\right] E_p(t) = \frac{\gamma_{ep}}{2} E_{ep}(t) +$$
$$-\frac{\omega_p}{\omega_s}\frac{k_p}{k_s}\left[G(\delta) - i\frac{\delta}{\gamma_{ab}} G(\delta)\right] |E_s(t)|^2 E_p(t), \tag{2.67a}$$

$$\dot{E}_s(t) + \left[\frac{\gamma_{cs}}{2} - i(n_s\omega_s - \omega_{cs})\right] E_s(t) =$$
$$\left[G(\delta) + i\frac{\delta}{\gamma_{ab}} G(\delta)\right] |E_p(t)|^2 E_s(t), \tag{2.67b}$$

where the refractive indexes $n_p = 1 + N\hbar a_p/\epsilon_0$ and $n_s = 1 + N\hbar a_s/\epsilon_0$ [see Eq. (2.53)] have been substituted.

Next the complex fields can be separated into their amplitudes and phases in the forms

$$E_p(t) = |E_p(t)|e^{-i\phi_p(t)}, \quad E_{ep}(t) = |E_{ep}(t)|e^{-i\phi_p(t)}; \tag{2.68a}$$

$$E_s(t) = |E_s(t)|e^{-i\phi_s(t)}. \tag{2.68b}$$

Here we suppose that the intracavity pump field always has the same phase with the incident pump field. This is valid for the continuous-wave and single-frequency incident light whose phase change is slower than the cavity's response time. By substituting Eqs. (2.68) into (2.67), two sets of equations, one for the field amplitudes and one for their phases/frequencies, can be obtained.

Field amplitude equation and the steady-state oscillation condition

Substituting Eqs. (2.68) into (2.67), the real parts give the equations of motion for the pump and Stokes field amplitudes:

$$|\dot{E}_p(t)| + \frac{\gamma_{cp}}{2}|E_p(t)| = -\frac{\omega_p}{\omega_s}\frac{k_p}{k_s}G(\delta)|E_s(t)|^2|E_p(t)| + \frac{\gamma_{ep}}{2}|E_{ep}(t)|, \tag{2.69a}$$

$$|\dot{E}_s(t)| + \frac{\gamma_{cs}}{2}|E_s(t)| = G(\delta)|E_p(t)|^2|E_s(t)|. \tag{2.69b}$$

We first give the steady-state solutions. At steady state, all the time derivatives are set to be zero. We solve Eqs.(2.69a) and (2.69b) algebraically to obtain that when the laser is above threshold,

$$|E_p|_{ss} = \sqrt{\frac{\gamma_{cs}}{2G(\delta)}}, \tag{2.70}$$

$$|E_s|_{ss} = \sqrt{\frac{\omega_s}{\omega_p}\frac{k_s}{k_p}\frac{\gamma_{ep}|E_{ep}|/|E_p|_{ss} - \gamma_{cp}}{2G(\delta)}}. \tag{2.71}$$

When the numerator in Eq.(2.71) equals zero, the laser's threshold is found to be

$$|E_{ep}|_{\text{threshold}} = \frac{\gamma_{cp}}{\gamma_{ep}}|E_p|_{ss}. \tag{2.72}$$

In the non-steady-state regime, Eqs.(2.69a) and (2.69b) needs to be numerically solved. The results will be given in a later section, or can also be found in Ref. [21]. Here we only give a simple view of the Stokes transient growth by adopting a trial solution of the form

$$|E_s(t)| = |E_s(0)|e^{gt}, \tag{2.73}$$

where g represents an exponential growth rate for Stokes. We substitute this form into Eq. (2.69b) and find g satisfies

$$g = G(\delta)|E_p|^2 - \frac{\gamma_{cs}}{2}. \tag{2.74}$$

If $E_p = E_{p,ss} = \sqrt{\gamma_{cs}/2G(\delta)}$ then $g = 0$, and the laser will be running in the steady-state; however once $E_p > E_{p,ss}$ the Stokes light will experience exponential growth, which will deplete the pump until $E_p = E_{p,ss}$ is again satisfied. In other words, Eq. (2.70) can be viewed as the steady-state oscillation condition:

$$\text{Saturated gain} = \text{Cavity loss};$$

$$G(\delta)|E_p|^2 = \frac{\gamma_{cs}}{2}. \tag{2.75}$$

This understanding will be helpful when we analyze the Stokes mode-hop hysteresis in a later chapter.

Frequency pulling

Substituting Eqs. (2.68) into (2.67), the imaginary parts give the frequency-determining equations:

$$\omega_p + \dot{\phi}_p = \omega_{cp} - (n_p - 1)\omega_p - \frac{\omega_p}{\omega_s}\frac{k_p}{k_s}G(\delta)|E_s(t)|^2\frac{\delta}{\gamma_{ab}}, \tag{2.76a}$$

$$\omega_s + \dot{\phi}_s = \omega_{cs} - (n_s - 1)\omega_s - G(\delta)|E_p(t)|^2\frac{\delta}{\gamma_{ab}}. \tag{2.76b}$$

Since $\omega_p \approx \omega_{cp}$, we can rewrite the term $\omega_{cp} - (n_p - 1)\omega_p$ in Eq. (2.76a):

$$\begin{aligned}\omega_{cp} - (n_p - 1)\omega_p &\approx \omega_{cp}[1 - (n_p - 1)] \\ &\approx \frac{\omega_{cp}}{1 + (n_p - 1)} \\ &= \frac{\omega_{cp}}{n_p}.\end{aligned} \tag{2.77}$$

Similarly, $\omega_{cs} - (n_s - 1)\omega_s \approx \omega_{cs}/n_s$ [6] in Eq. (2.76b). By using these approximations and then substituting Eqs. (2.70) and (2.71), Eqs. (2.76) give that at steady-state and above threshold, the *required* oscillating frequencies are

$$\begin{aligned}\omega_p + \dot{\phi}_p &= \frac{\omega_{cp}}{n_p} + \frac{\delta}{2}\frac{\gamma_{cp}}{\gamma_{ab}} - \frac{\delta}{2}\frac{\gamma_{ep}}{\gamma_{ab}}\frac{|E_{ep}|}{|E_p|_{ss}} \\ &= \frac{\omega_{cp}}{n_p} + \left[1 - \sqrt{\mathcal{R}(\delta)}\right]\frac{\delta}{2}\frac{\gamma_{cp}}{\gamma_{ab}},\end{aligned} \tag{2.78a}$$

$$\omega_s + \dot{\phi}_s = \frac{\omega_{cs}}{n_s} - \frac{\delta}{2}\frac{\gamma_{cs}}{\gamma_{ab}}, \tag{2.78b}$$

where $\sqrt{\mathcal{R}(\delta)} = |E_{ep}|/|E_{ep}|_{\text{threshold}}(\delta)$ is the field pumping rate which is a function of the two-photon-detuning. We first note that although the steady-state solution

[6] When $|x| \ll 1$, $1 - x^2 \approx 1$, this is equivalent to $1 - x \approx 1/(1 + x)$. Here $x = n_{p(s)} - 1$.

means $d/dt \equiv 0$ for all amplitude quantities, steady state can still mean $d\phi/dt =$ constant [25, page 948], which means a constant frequency. Therefore, while the reference frequencies $\omega_{p(s)}$ were arbitrarily chosen when we derived the wave equations using the slowly varying envelope approximation in Section 2, Eqs. (2.78) reveal that the *required* oscillating frequencies $\omega_{p(s)} + \dot{\phi}_{p(s)}$ are different from the "cold" cavity resonant frequencies $\omega_{cp(s)}$. (We could choose $\omega_{p(s)} = \omega_{cp(s)}$ from the beginning, then $\dot{\phi}_{p(s)}$ will be the required frequency shifts or the amount of frequency-pulling).

The first term at the right-hand-side of Eq. (2.78a) or (2.78b) is the frequency-pulling due to the single-photon-induced dispersion. It simply means that the resonances of a vacuum cavity (ω_{cq}) should be modified if there is any medium inside the cavity (divided by medium's refractive index n_q).

The second term proportional to the two-photon-detuning δ in Eqs. (2.78) is the frequency-pulling due to the Raman-induced dispersion. Let us estimate how large the Raman frequency-pulling is. For typical cw Raman lasers $\gamma_{cp,s}/2\pi \sim 0.01 - 1$ MHz and $\gamma_{ab}/2\pi$ is around several hundred MHz, the amount of pulling is in the range $(10^{-5} \sim 10^{-3}) \times \delta$. Usually the two-photon-detuning $\delta/2\pi$ is less than ± 1 GHz, so the amount of pulling is in the kHz range. Using Eqs. (2.78), we calculate the amounts of frequency-pulling in a real vibrational Raman laser and plot the results in Fig. 5.

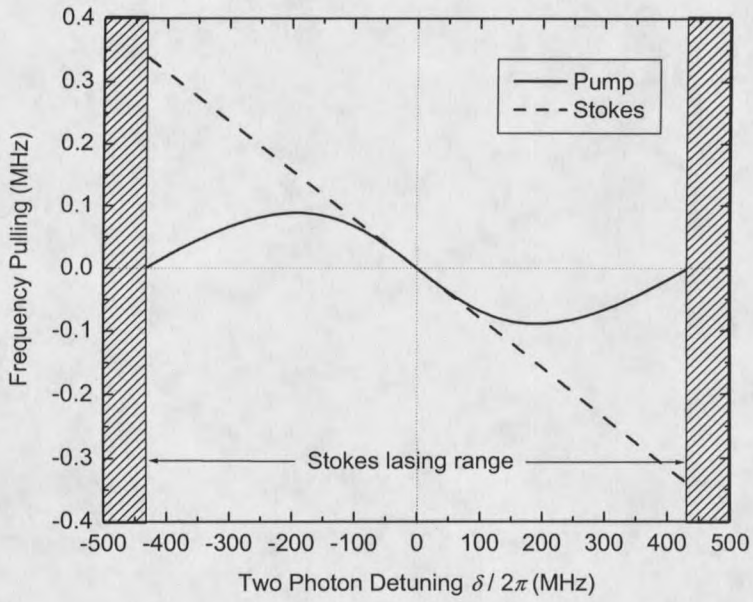

Figure 5 Theoretical calculation of the amount of frequency-pulling $\dot{\phi}$ as a function of two-photon-detuning δ in a cw vibrational Raman laser. Solid line: pump; dashed line: Stokes. Parameters used are: $\lambda_p = 792\,\text{nm}$; $\lambda_s = 1180\,\text{nm}$; $\alpha_g = 1.5 \times 10^{-9}\,\text{cm/W}$ (line-center value for 10 atm H_2 at 25°C); mirror transmittance $= 0.9999$; mirror absorption $= 30 \times 10^{-6}$; cavity length $= 7.62\,\text{cm}$; and pumping rate is at four times the line-center threshold. In the two shaded areas, the Stokes laser is below threshold.

In reality, the cavity is frequency-locked to the pump laser. Usually the pump laser is frequency tuned and the locking servos are able to follow and maintain the locking. Once the system is tuned off the line-center ($\delta \neq 0$), the PZT servo will find a ω_{cp} value to compensate the frequency-pulling in Eq. (2.78a), while the lasing Stokes frequency ω_s will adjust itself to satisfy Eq. (2.78b).

In terms of pump and Stokes powers

It is necessary to write the intracavity field equations in terms of measurable powers so that we can compare the experimental data with the theory. From Eqs. (2.12)

and (2.62) one can see that $E_q(t)$ represents the peak field-amplitude of the intracavity standing-wave in space (i.e., at the center of the TEM_{00} transverse profile and at the antinodes of the standing-wave along the longitudinal direction). The intracavity light intensity (optical power per unit area, or power density, on the plane perpendicular to the z-axis) is calculated by [34, page 50]

$$I_q = \frac{v_q \epsilon_q}{2} |E_q(t) u_q(\mathbf{r})|^2, \tag{2.79}$$

where $v_q = c/n_q$ is the intracavity light speed and $\epsilon_q = n_q^2 \epsilon_0$ is the dielectric permeability of the intracavity medium. The intracavity power along the longitudial direction can be calculated (we use Π to denote the intracavity power and use P to denote the power outside the cavity):

$$\begin{aligned} \Pi_q'(z,t) &= \int_0^\infty r dr \int_0^{2\pi} d\phi I_q \\ &= \frac{\pi w_{0q}^2 n_q}{4} \sqrt{\frac{\epsilon_0}{\mu_0}} |E_q(t)|^2 \frac{\sin^2(k_q z)}{1 + (2z/b_q)^2}, \end{aligned} \tag{2.80}$$

where $w_{0q} = \sqrt{b_q/k_q}$ is the radius at the beam waist. If the beam inside the cavity is collimated ($z \ll b_q$), the peak intracavity power along the longitudinal direction (at the antinode planes of the standing-wave) is given by

$$\begin{aligned} \Pi_q(t) &= \frac{\pi w_{0q}^2 n_q}{4} \sqrt{\frac{\epsilon_0}{\mu_0}} |E_q(t)|^2 \\ &= \frac{\pi b_q}{4 \omega_q \mu_0} |E_q(t)|^2. \end{aligned} \tag{2.81}$$

A standing-wave consists of two counter-propagating equal-amplitude traveling-waves and the peak-amplitude ratio between the standing and traveling waves is 2:1. Therefore the optical power of the traveling-waves (or so-called cavity circulating power) is

equal to $\frac{1}{4}\Pi_q(t)$.

Using the relation Eq. (2.81), one can convert Eqs. (2.69) into

$$\dot{\Pi}_p(t) + \gamma_{cp}\Pi_p(t) = -\frac{8\omega_p\mu_0}{\pi b}\frac{k_p}{k_s}G(\delta)\Pi_s(t)\Pi_p(t) + \gamma_{ep}\sqrt{\Pi_p(t)\mathrm{P}_{ep}(t)}, \tag{2.82a}$$

$$\dot{\Pi}_s(t) + \gamma_{cs}\Pi_s(t) = \frac{8\omega_p\mu_0}{\pi b}G(\delta)\Pi_p(t)\Pi_s(t). \tag{2.82b}$$

The steady-state solutions are

$$\Pi_{p,ss} = \frac{\pi b}{4\omega_p\mu_0}\frac{\gamma_{cs}}{2G(\delta)}, \tag{2.83}$$

$$\Pi_{s,ss} = \frac{\pi b}{4\omega_p\mu_0}\frac{k_s}{k_p}\frac{1}{2G(\delta)}\left[\gamma_{ep}\sqrt{\frac{\mathrm{P}_{ep}}{\Pi_{p,ss}}} - \gamma_{cp}\right]. \tag{2.84}$$

The threshold pump power is given by

$$\mathrm{P}_{ep,\mathrm{th}} = \left(\frac{\gamma_{cp}}{\gamma_{ep}}\right)^2\Pi_{p,ss} = \frac{(\ln\sqrt{R_{1p}R_{2p}})^2}{4T_{1p}}\Pi_{p,ss} \tag{2.85}$$

Note again that $\Pi_p(t)$ and $\Pi_s(t)$ are the peak intracavity powers along the longitudinal direction (at the antinodes of the standing-wave). Because the cavity circulating power is equal to $\frac{1}{4}\Pi_q(t)$, the time-averaged powers measured just outside the cavity mirrors take the following forms [23, 21]:

$$\text{Reflected pump}: \quad \mathrm{P}_{1p} = R_{1p}\mathrm{P}_{ep} + \frac{1}{4}T_{1p}\Pi_p - \sqrt{R_{1p}\mathrm{P}_{ep}}\sqrt{T_{1p}\Pi_p}, \tag{2.86a}$$

$$\text{Transmitted pump}: \quad \mathrm{P}_{2p} = \frac{1}{4}T_{2p}\Pi_p, \tag{2.86b}$$

$$\text{Front Stokes}: \quad \mathrm{P}_{1s} = \frac{1}{4}T_{1s}\Pi_s, \tag{2.86c}$$

$$\text{Back Stokes}: \quad \mathrm{P}_{2s} = \frac{1}{4}T_{2s}\Pi_s. \tag{2.86d}$$

Here "front" means the side at which the pump laser enters the cavity; then the other side of the cavity is named "back". The first equation shows that the total reflected pump field is an interference between the first reflection and the cavity leakage field.

Numerical time-dependent solution

For the time-dependent solution to the cw Stokes laser, we choose to numerically solve the complex field equations (2.67) using MATHEMATICA [35] (The code is given in Appendix B). This work was first done by Brasseur [23, 21].

We numerically solve Eqs (2.67) for the vibrational transition of 792→1180 nm. Therefore the gain and the linewidth used are $\alpha_g = 1.5 \times 10^{-9}$cm/W (line-center value for 10 atm H_2 at 25°C)[2] and $\gamma_{abv}/2\pi = 250$ MHz (HWHM; for 10 atm H_2 at 25°C)[3]. The following cavity parameters are used: $R = 0.9999$ (mirror reflectance) and $A = 30 \times 10^{-6}$ (mirrors' power loss) for both mirrors at both wavelengths; $L = 7.62$ cm (cavity length); $r = 50$ cm (mirrors' radius of curvature) for both mirrors. In addition, we choose the reference frequency $\omega_{p(s)} = \omega_{cp(s)}/n_{p(s)}$ to simplify the calculation.

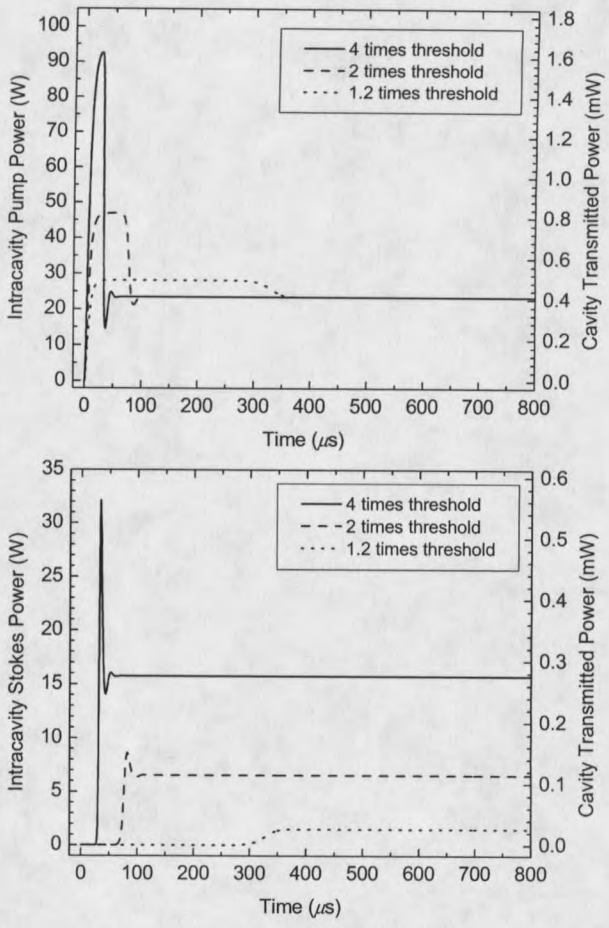

Figure 6 Numerical simulation of the "turn-on" behavior in a cw vibrational Raman laser at different pumping rates. The pump (top) and the Stokes (bottom) powers are plotted as functions of time. The solid line is at a pumping rate of 4 times the threshold; the dashed line is at 2 times the threshold; and the dotted line is at 1.2 times the threshold. All the curves are at the Raman gain line-center (i.e., the two-photon-detuning $\delta = 0$). The left horizontal axis is the intracavity spatial peak power and the right axis is the cavity transmitted power (single end).

The first time-dependent result is given in Fig. 6. The field amplitudes of the pump and the Stokes are numerically calculated as functions of time. We then convert them into optical powers using Eq. (2.81). Three cases of different pumping rates (all on the Raman resonance) are calculated and plotted. It can be seen that at low pumping rate of 1.2 times the threshold, the laser turns on smoothly and slowly with

nearly no relaxation oscillations; whereas at 4 times the threshold, there is a large overshoot followed by some oscillations.

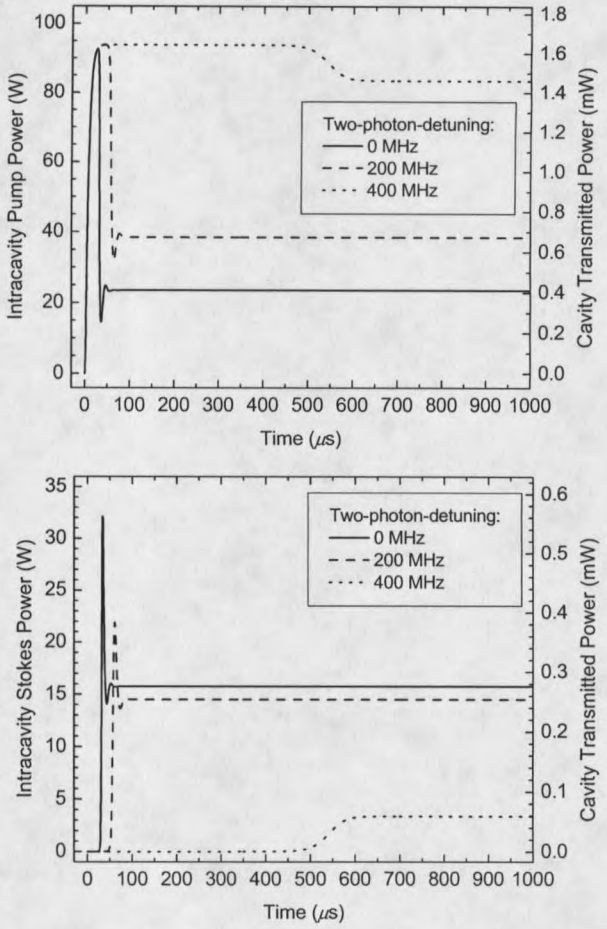

Figure 7 Numerical simulation of the "turn-on" behavior in a cw vibrational Raman laser at different detunings. The pump (top) and the Stokes (bottom) powers are plotted as functions of time. The solid line is when the two-photon-detuning $\delta/2\pi = 0$; the dashed line is when $\delta/2\pi = 200$ MHz; and the dotted line is when $\delta/2\pi = 400$ MHz. All the curves are at the pumping rate of 4 times the line-center threshold. The left horizontal axis is the intracavity spatial peak power and the right axis is the cavity transmitted power (single end).

Fig. 7 gives another comparison of the "turn-on" behaviors. This time, while the input pump power is fixed at 4 times the line-center threshold, the field amplitudes

are calculated at three different two-photon-detunings. Similar to Fig. 6, as the laser is detuned away from the Raman resonance by 400 MHz, it starts smoothly and slowly due to the weaker pumping rate (the threshold increases as detuned away); whereas as the laser is on or near the Raman resonance (now it is pumped harder), there are dramatic dynamics before steady state is achieved.

Fig. 6 and Fig. 7 explain our experimental experiences. If the pumping rate is high, it is difficult to stabilize the pump laser to the cavity because of the dramatic turn-on dynamics of the Stokes generation. The way to make the cw Raman laser run is to lock the pump laser and the cavity together at the low pumping rate or even below the threshold. Then the steady-state lasing can be approached at high pumping rates by slowly increasing the pump power or tuning to the line-center.

It is interesting to note that, when we numerically solve the differential field equations, an initial condition of nonzero Stokes power must be chosen to make the Stokes laser oscillate. This can be viewed as the requirement of the stimulated Raman scattering: some seeding Stokes photons are necessary for the Stokes amplification. In our cw Raman laser, the Stokes oscillation is "self-seeded" from the spontaneous Raman scattering. In the above numerical solutions, we have chosen the circulating power in a single-photon cavity ($\sim 0.3\,\mathrm{nW}$) as the initial condition.

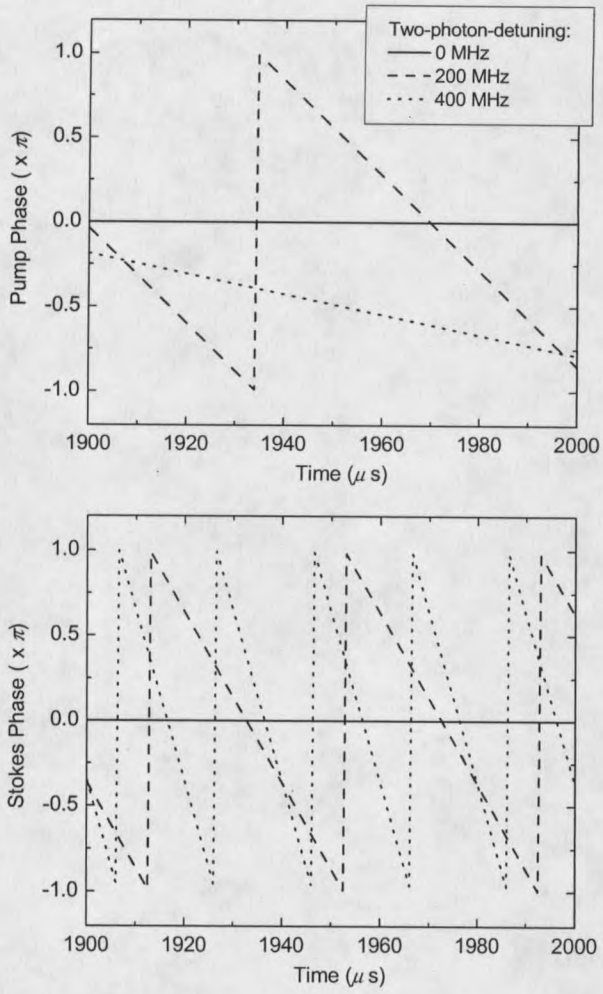

Figure 8 After the cw Raman laser in Fig. 7 grows into steady-state (note the horizontal time scale), the calculated phase evolutions of the pump (top) and the Stokes (bottom) beams are shown for different detunings. The slope of the phase curve gives the amount of frequency-pulling.

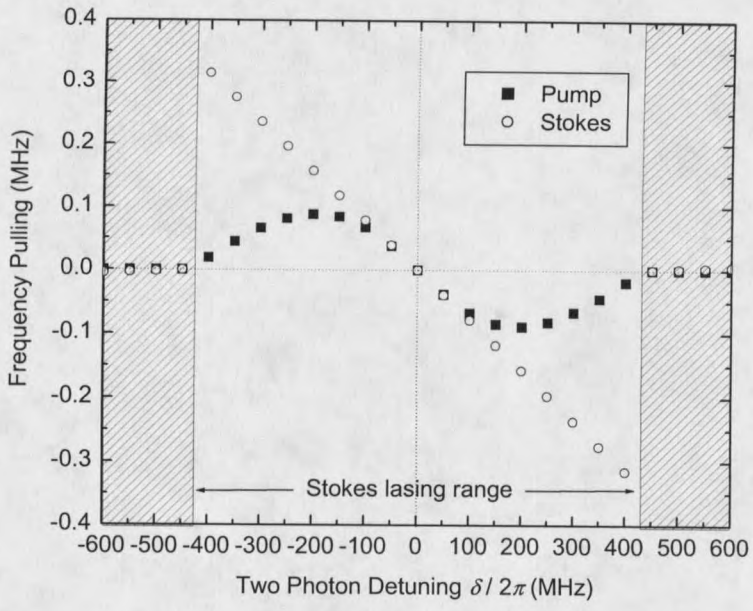

Figure 9 The slopes of the phase curves in Fig. 7 as functions of the two-photon-detunings. This numerical calculation agrees with the theoretical plot in Fig. 5.

Numerically solving the complex field equations (2.67) can also give the phase dynamics of the pump and the Stokes fields. Fig. 8 shows that at steady-state, if the two-photon-detuning is zero, the phases of the two fields are constantly zero with time, meaning $\omega_{p(s)} = \omega_{cp(s)}/n_{p(s)}$ or no frequency pulling caused by the two-photon dispersion. However, if the Stokes resonance is detuned away from the Raman line-center, the phases of both the pump and Stokes fields change linearly with time, or $\dot{\phi}_{p(s)}$ = constant, in steady state. The slope of the phase curve $\dot{\phi}_{p(s)}$ gives the amount of frequency-pulling. Clearly, Fig. 8 shows that this slope is dependent on the two-photon-detuning. We numerically calculate the slope at different two-photon-detunings and plot the dependence in Fig. 9. We obtained the same result from the analytic steady-state solutions plotted in Fig. 5. This agreement proves the

correctness of our numerical time-dependent solutions.

The Anti-Stokes Emission

We consider three fields in this section: $q = 0$ (pump), $q = -1$ (Stokes), and $q = 1$ (anti-Stokes), as exactly shown in Fig. 2. In this situation, besides the two-photon Raman interactions, there also exists a four-wave mixing process, by which the Stokes and anti-Stokes fields can be strongly coupled. To develop the theory, we assume a triple-resonance condition (i.e., all the three fields are resonant with the cavity), although in reality this condition will be experimentally difficult due to dispersion effects. At the end of this section we will estimate the dispersion and discuss the methods to compensate it.

Complex field equations

Using the subscripts p, s, and a to represent the pump, Stokes, and anti-Stokes fields respectively, from Eq. (2.14) we have three field equations:

$$\dot{E}_p(t) + \left[\frac{\gamma_{cp}}{2} - i(\omega_p - \omega_{cp})\right] E_p(t) = \frac{\gamma_{ep}}{2} E_{ep}(t) + i\frac{\omega_p}{2\epsilon_0}\frac{1}{V_p}\iiint_{\text{cavity}} dxdydz P_p(\mathbf{r},t) u_p^*(\mathbf{r}), \quad (2.87a)$$

$$\dot{E}_s(t) + \left[\frac{\gamma_{cs}}{2} - i(\omega_s - \omega_{cs})\right] E_s(t) = i\frac{\omega_s}{2\epsilon_0}\frac{1}{V_s}\iiint_{\text{cavity}} dxdydz P_s(\mathbf{r},t) u_s^*(\mathbf{r}), \quad (2.87b)$$

$$\dot{E}_a(t) + \left[\frac{\gamma_{ca}}{2} - i(\omega_a - \omega_{ca})\right] E_a(t) = i\frac{\omega_a}{2\epsilon_0}\frac{1}{V_a}\iiint_{\text{cavity}} dxdydz P_a(\mathbf{r},t) u_a^*(\mathbf{r}). \quad (2.87c)$$

The three polarization terms are given by Eq. (2.38):

$$P_p(\mathbf{r},t) = 2N\hbar\left[a_p E_p(t)u_p(\mathbf{r}) + d_0\rho_{ba}(\mathbf{r},t)E_s(t)u_s(\mathbf{r}) + d_0\rho_{ab}(\mathbf{r},t)E_a(t)u_a(\mathbf{r})\right], \tag{2.88a}$$

$$P_s(\mathbf{r},t) = 2N\hbar\left[a_s E_s(t)u_s(\mathbf{r}) + d_0\rho_{ab}(\mathbf{r},t)E_p(t)u_p(\mathbf{r})\right], \tag{2.88b}$$

$$P_a(\mathbf{r},t) = 2N\hbar\left[a_a E_a(t)u_a(\mathbf{r}) + d_0\rho_{ba}(\mathbf{r},t)E_p(t)u_p(\mathbf{r})\right], \tag{2.88c}$$

where we have made the approximation that $d_p \approx d_s \approx d_0$ and both d's are real. We again take the fact that the population is nearly undepleted from the ground state so that the population equation (2.40a) can be dropped. The steady-state coherence Eq. (2.45b) now has the form

$$\begin{aligned}\rho_{ab} &= \frac{i\Omega_{ab}D}{\gamma_{ab} - i\delta} \\ &= i\frac{d_0}{2}D\frac{E_s(t)u_s(\mathbf{r})E_p^*(t)u_p^*(\mathbf{r}) + E_p(t)u_p(\mathbf{r})E_a^*(t)u_a^*(\mathbf{r})}{\gamma_{ab} - i\delta},\end{aligned} \tag{2.89}$$

where the relative Stark shift $\Omega_{aa} - \Omega_{bb}$ has been ignored. With Eqs. (2.88) and (2.89) (again using the adiabatic following approximation), Eqs. (2.87) become

$$\begin{aligned}\dot{E}_p + \left[\frac{\gamma_{cp}}{2} - i\left(\omega_p - \omega_{cp}\right)\right]E_p &= \frac{\gamma_{ep}}{2}E_{ep} + i\omega_p\frac{N\hbar a_p}{\epsilon_0}\frac{V_p}{V_p}E_p \\ &+ \omega_p\frac{N\hbar d_0^2 D}{2\epsilon_0}\frac{1}{\gamma_{ab} + i\delta}\frac{1}{V_p}(V_{ps}|E_s|^2E_p + V_{\mathrm{FWM}}E_p^*E_sE_a) \\ &- \omega_p\frac{N\hbar d_0^2 D}{2\epsilon_0}\frac{1}{\gamma_{ab} - i\delta}\frac{1}{V_p}(V_{pa}|E_a|^2E_p + V_{\mathrm{FWM}}E_p^*E_sE_a),\end{aligned} \tag{2.90a}$$

$$\begin{aligned}\dot{E}_s + \left[\frac{\gamma_{cs}}{2} - i\left(\omega_s - \omega_{cs}\right)\right]E_s &= i\omega_s\frac{N\hbar a_s}{\epsilon_0}\frac{V_s}{V_s}E_s \\ &- \omega_s\frac{N\hbar d_0^2 D}{2\epsilon_0}\frac{1}{\gamma_{ab} - i\delta}\frac{1}{V_s}(V_{ps}|E_p|^2E_s + V_{\mathrm{FWM}}E_pE_pE_a^*),\end{aligned} \tag{2.90b}$$

$$\dot{E}_a + \left[\frac{\gamma_{ca}}{2} - i\left(\omega_a - \omega_{ca}\right)\right] E_a = i\omega_a \frac{N\hbar a_a}{\epsilon_0}\frac{V_a}{V_a}E_a$$
$$+ \omega_a \frac{N\hbar d_0^2 D}{2\epsilon_0}\frac{1}{\gamma_{ab}+i\delta}\frac{1}{V_a}(V_{pa}|E_p|^2 E_a + V_{\mathrm{FWM}}E_p E_p E_s^*), \qquad (2.90c)$$

where the cavity's single mode-volumes V_p, V_s and V_a and the Raman overlap mode-volumes V_{ps} and V_{pa} are given by

$$V_{p(s,a)} = 2\pi\int_{-L/2}^{L/2} dz \int_0^\infty r dr |u_{p(s,a)}|^2 = 2\pi\frac{L}{8}\frac{b}{k_{p(s,a)}}, \qquad (2.91a)$$

$$V_{ps(pa)} = 2\pi\int_{-L/2}^{L/2} dz \int_0^\infty r dr |u_p|^2 |u_{s(a)}|^2 = \frac{2\pi}{16}\frac{b^2}{k_p + k_{s(a)}}\tan^{-1}\left(\frac{L}{b}\right). \qquad (2.91b)$$

There is also a four-wave-mixing (FWM) mode-volume V_{FWM} that is given by the integral

$$V_{\mathrm{FWM}} = 2\pi\int_{-L/2}^{L/2} dz \int_0^\infty r dr u_p^2 u_s^* u_a^*. \qquad (2.92)$$

The integral is difficult to calculate unless we use the collimated-beam-approximation so that the phase of the intracavity wavefront has no z-dependence:

$$u_q(r,z) = e^{-r^2 k_q/b}\sin(k_q z). \qquad (2.93)$$

With this approximation we can calculate that

$$V_{\mathrm{FWM}} = 2\pi\frac{1}{8}\frac{b}{\sum k}\frac{\sin(\Delta k L/2)}{\Delta k}, \qquad (2.94)$$

where $\sum k = 2k_p + k_s + k_a$ and $\Delta k = 2k_p - k_s - k_a$. We substitute this result along with Eqs. (2.91) (applying the approximation Eq.(2.66)) to obtain

$$\dot{E}_p + \left\{\frac{\gamma_{cp}}{2} - i\left[\left(\frac{N\hbar a_p}{\epsilon_0}+1\right)\omega_p - \omega_{cp}\right]\right\} E_p = \frac{\gamma_{ep}}{2}E_{ep}$$
$$+\omega_p\frac{N\hbar d_0^2 D}{2\epsilon_0}\frac{1}{\gamma_{ab}+i\delta}\frac{1}{2}\left[\frac{k_p}{k_p+k_s}|E_s|^2 E_p + \frac{k_p}{\sum k}\frac{\sin(\Delta k L/2)}{\Delta k L/2}E_p^* E_s E_a\right]$$
$$-\omega_p\frac{N\hbar d_0^2 D}{2\epsilon_0}\frac{1}{\gamma_{ab}-i\delta}\frac{1}{2}\left[\frac{k_p}{k_p+k_a}|E_a|^2 E_p + \frac{k_p}{\sum k}\frac{\sin(\Delta k L/2)}{\Delta k L/2}E_p^* E_s E_a\right], \qquad (2.95a)$$

$$\dot{E}_s + \left\{ \frac{\gamma_{cs}}{2} - i \left[(\frac{N\hbar a_s}{\epsilon_0} + 1)\omega_s - \omega_{cs} \right] \right\} E_s =$$
$$-\omega_s \frac{N\hbar d_0^2 D}{2\epsilon_0} \frac{1}{\gamma_{ab} - i\delta} \frac{1}{2} \left[\frac{k_s}{k_p + k_s} |E_p|^2 E_s + \frac{k_s}{\sum k} \frac{\sin(\Delta kL/2)}{\Delta kL/2} E_p E_p E_a^* \right], \quad (2.95b)$$

$$\dot{E}_a + \left\{ \frac{\gamma_{ca}}{2} - i \left[(\frac{N\hbar a_a}{\epsilon_0} + 1)\omega_a - \omega_{ca} \right] \right\} E_a =$$
$$\omega_a \frac{N\hbar d_0^2 D}{2\epsilon_0} \frac{1}{\gamma_{ab} + i\delta} \frac{1}{2} \left[\frac{k_a}{k_p + k_a} |E_p|^2 E_a + \frac{k_a}{\sum k} \frac{\sin(\Delta kL/2)}{\Delta kL/2} E_p E_p E_s^* \right]. \quad (2.95c)$$

Let us write these equations in simpler forms. First, as discussed in page 32, the reference frequencies $\omega_{p(s,a)}$ can be arbitrarily chosen. Thus we can choose them to make $(N\hbar a_q/\epsilon_0 + 1)\omega_q - \omega_{cq} = 0$ $(q = p, s, a)$. Second, we define a coupling coefficient

$$C_c = \frac{k_p + k_s}{\sum k} \frac{\sin(\Delta kL/2)}{\Delta kL/2}, \quad (2.96)$$

and use the gain factor $G(\delta)$ defined by Eq. (2.65):

$$G(\delta) = -\frac{1}{4}\omega_s \frac{N\hbar d_0^2 D}{\epsilon_0} \frac{\gamma_{ab}}{\gamma_{ab}^2 + \delta^2} \frac{\lambda_p}{\lambda_p + \lambda_s} \frac{\tan^{-1}(L/b)}{L/b}$$
$$\approx -\frac{1}{4}\omega_s \frac{N\hbar d_0^2 D}{\epsilon_0} \frac{\gamma_{ab}}{\gamma_{ab}^2 + \delta^2} \frac{\lambda_p}{\lambda_p + \lambda_s}. \quad (2.97)$$

Eqs. (2.95) then become

$$\dot{E}_p + \frac{\gamma_{cp}}{2} E_p = \frac{\gamma_{ep}}{2} E_{ep} - \frac{\omega_p}{\omega_s} \frac{k_p}{k_s} G(\delta)(1 - \frac{i\delta}{\gamma_{ab}}) \left[|E_s|^2 E_p + C_c E_p^* E_s E_a \right]$$
$$+ \frac{\omega_p}{\omega_s} \frac{k_p}{k_s} G(\delta)(1 + \frac{i\delta}{\gamma_{ab}}) \left[\frac{k_p + k_s}{k_p + k_a} |E_a|^2 E_p + C_c E_p^* E_s E_a \right], \quad (2.98a)$$

$$\dot{E}_s + \frac{\gamma_{cs}}{2} E_s = G(\delta)(1 + \frac{i\delta}{\gamma_{ab}}) \left[|E_p|^2 E_s + C_c E_p E_p E_a^* \right], \quad (2.98b)$$

$$\dot{E}_a + \frac{\gamma_{ca}}{2} E_a = -\frac{\omega_a}{\omega_s} \frac{k_a}{k_s} G(\delta)(1 - \frac{i\delta}{\gamma_{ab}}) \left[\frac{k_p + k_s}{k_p + k_a} |E_p|^2 E_a + C_c E_p E_p E_s^* \right]. \quad (2.98c)$$

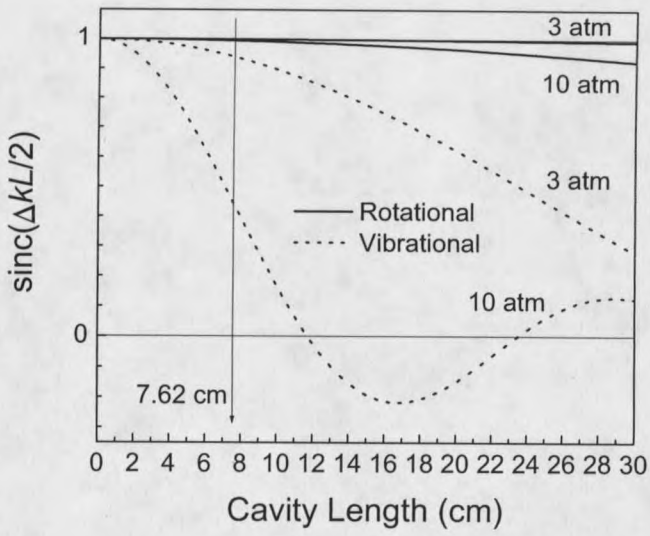

Figure 10 The values of $\mathrm{sinc}(\Delta kL/2) = \frac{\sin(\Delta kL/2)}{\Delta kL/2}$ as a function of cavity length. We plotted for $\lambda_p = 792$ nm, $\lambda_s = 830$ nm in the rotational transition and $\lambda_s = 1180$ nm in the vibrational transition at two different H_2 pressures. When the H_2 pressure is 10 atm (3 atm), $\Delta k \approx -4.6\ \mathrm{m}^{-1}$ $(-1.4\ \mathrm{m}^{-1})$ for the rotational transition and $\Delta k \approx -54\ \mathrm{m}^{-1}$ $(-16\ \mathrm{m}^{-1})$ for the vibrational transition. 7.62 cm (3 in) is the cavity length we have used in the demonstrated cw Stokes laser systems.

Note that E_p, E_s and E_a are all complex fields. We separate them into their amplitudes and phases in the forms

$$E_p(t) = |E_p(t)|e^{-i\phi_p(t)}, \qquad E_{ep}(t) = |E_{ep}(t)|e^{-i\phi_p(t)}; \tag{2.99a}$$

$$E_s(t) = |E_s(t)|e^{-i\phi_s(t)}. \tag{2.99b}$$

$$E_a(t) = |E_a(t)|e^{-i\phi_a(t)}. \tag{2.99c}$$

Substituting them into Eqs. (2.98), the real parts give equations for field amplitudes:

$$|\dot{E}_p| + \frac{\gamma_{cp}}{2}|E_p| = \frac{\gamma_{ep}}{2}|E_{ep}| - \frac{\omega_p}{\omega_s}\frac{k_p}{k_s}G(\delta)\left[|E_s|^2|E_p| - \frac{k_p + k_s}{k_p + k_a}|E_a|^2|E_p|\right] - 2\frac{\omega_p}{\omega_s}\frac{k_p}{k_s}C_c G(\delta)|E_p||E_s||E_a|\frac{\delta}{\gamma_{ab}}\sin(\Delta\phi), \tag{2.100a}$$

$$|\dot{E}_s| + \frac{\gamma_{cs}}{2}|E_s| = G(\delta)|E_p|^2|E_s| + C_c G(\delta)|E_p||E_p||E_a|\left[\cos(\Delta\phi) + \frac{\delta}{\gamma_{ab}}\sin(\Delta\phi)\right], \tag{2.100b}$$

$$|\dot{E}_a| + \frac{\gamma_{ca}}{2}|E_a| = -\frac{\omega_a}{\omega_s}\frac{k_a}{k_s}G(\delta)\frac{k_p + k_s}{k_p + k_a}|E_p|^2|E_a| - \frac{\omega_a}{\omega_s}\frac{k_a}{k_s}C_c G(\delta)|E_p||E_p||E_s|\left[\cos(\Delta\phi) - \frac{\delta}{\gamma_{ab}}\sin(\Delta\phi)\right]. \tag{2.100c}$$

The imaginary parts give equations for the frequency pulling:

$$\dot{\phi}_p = -\frac{\omega_p}{\omega_s}\frac{k_p}{k_s}G(\delta)\left[|E_s|^2 + \frac{k_p + k_s}{k_p + k_a}|E_a|^2\right]\frac{\delta}{\gamma_{ab}} - 2\frac{\omega_p}{\omega_s}\frac{k_p}{k_s}C_c G(\delta)|E_s||E_a|\frac{\delta}{\gamma_{ab}}\cos(\Delta\phi), \tag{2.101a}$$

$$\dot{\phi}_s = -G(\delta)|E_p|^2\frac{\delta}{\gamma_{ab}} - C_c G(\delta)|E_p||E_p|\frac{|E_a|}{|E_s|}\left[\frac{\delta}{\gamma_{ab}}\cos(\Delta\phi) - \sin(\Delta\phi)\right], \tag{2.101b}$$

$$\dot{\phi}_a = -\frac{\omega_a}{\omega_s}\frac{k_a}{k_s}G(\delta)\frac{k_p + k_s}{k_p + k_a}|E_p|^2\frac{\delta}{\gamma_{ab}} - \frac{\omega_a}{\omega_s}\frac{k_a}{k_s}C_c G(\delta)|E_p||E_p|\frac{|E_s|}{|E_a|}\left[\frac{\delta}{\gamma_{ab}}\cos(\Delta\phi) + \sin(\Delta\phi)\right], \tag{2.101c}$$

where $\Delta\phi = 2\phi_p - \phi_s - \phi_a$ is the phase difference between the three waves.

Analytic steady-state solution for zero two-photon-detuning

When the two-photon-detuning $\delta = 0$, the Raman-induced dispersion equals zero and thus the frequency pulling $\dot{\phi}_p = \dot{\phi}_s = \dot{\phi}_a = 0$ (later our numerical solution will confirm this). Under this condition, from Eqs. (2.101) it is easy to see

$$\sin(\Delta\phi) = \sin(2\phi_p - \phi_s - \phi_a) = 0. \tag{2.102}$$

This still leaves an uncertainty of whether $\cos(\Delta\phi) = 1$ or -1. Let us examine Eq. (2.100c) at steady state. Since the field amplitude $|E_a|$ is non-negative, $\cos(\Delta\phi) = -1\,(+1)$ is then required when $C_c > 0\,(< 0)$, or

$$\Delta\phi = 2\phi_p - \phi_s - \phi_a = \begin{cases} (\text{odd integer}) \times \pi, & \text{if } C_c > 0; \\ (\text{even integer}) \times \pi, & \text{if } C_c < 0. \end{cases} \tag{2.103}$$

Therefore under the condition of zero two-photon-detuning, the field amplitude equations at steady state have the form

$$\frac{\gamma_{cp}}{2}|E_p| = -\frac{\omega_p}{\omega_s}\frac{k_p}{k_s}G(\delta)\left(|E_s|^2|E_p| - \frac{k_p + k_s}{k_p + k_a}|E_a|^2|E_p|\right) + \frac{\gamma_{ep}}{2}|E_{ep}(t)|, \tag{2.104a}$$

$$\frac{\gamma_{cs}}{2}|E_s| = G(\delta)\left(|E_p|^2|E_s| - |C_c||E_p||E_p||E_a|\right), \tag{2.104b}$$

$$\frac{\gamma_{ca}}{2}|E_a| = -\frac{\omega_a}{\omega_s}\frac{k_a}{k_s}G(\delta)\left(\frac{k_p + k_s}{k_p + k_a}|E_p|^2|E_a| - |C_c||E_p||E_p||E_s|\right). \tag{2.104c}$$

From Eqs. (2.104b) and (2.104c), we can eliminate $|E_p|^2$ to obtain

$$|C_c|\left(\frac{|E_a|}{|E_s|}\right)^2 - \left(\frac{\gamma_{cs}}{\gamma_{ca}}\frac{\omega_a}{\omega_s}\frac{k_a}{k_s}\frac{k_p + k_s}{k_p + k_a} + 1\right)\frac{|E_a|}{|E_s|} + \frac{\gamma_{cs}}{\gamma_{ca}}\frac{\omega_a}{\omega_s}\frac{k_a}{k_s}|C_c| = 0. \tag{2.105}$$

Let ξ denote the ratio $|E_a|/|E_s|$. Eq. (2.105) has two roots:

$$\xi_{\pm} = \frac{1}{2|C_c|}\left(\frac{\gamma_{cs}}{\gamma_{ca}}\frac{\omega_a}{\omega_s}\frac{k_a}{k_s}\frac{k_p+k_s}{k_p+k_a}+1\right) \pm \frac{1}{2|C_c|}\sqrt{\left(\frac{\gamma_{cs}}{\gamma_{ca}}\frac{\omega_a}{\omega_s}\frac{k_a}{k_s}\frac{k_p+k_s}{k_p+k_a}+1\right)^2 - 4\frac{\gamma_{cs}}{\gamma_{ca}}\frac{\omega_a}{\omega_s}\frac{k_a}{k_s}C_c^2}. \tag{2.106}$$

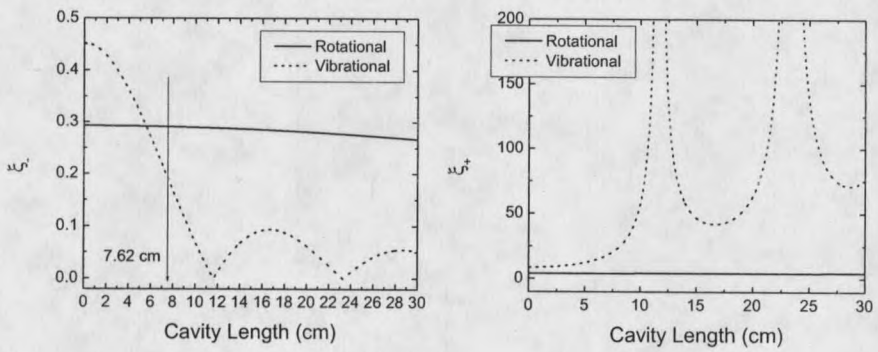

Figure 11 Values of ξ's are calculated as function of cavity length (left: ξ_-, right: ξ_+). ξ_+ is always larger than 1. 7.62 cm (3 in) is the cavity length we have used in the demonstrated systems. Parameters used for calculation are: $\lambda_p = 792$ nm, $\lambda_s = 830$ nm, $\lambda_a = 757$ nm (rotational), $\lambda_s = 1180$ nm, $\lambda_a = 596$ nm (vibrational), reflectance and absorption are 0.9999 and 30 ppm for both mirrors and all wavelengths, mirror radius of curvature is 50 cm, H_2 pressure is 10 atm, and $\Delta k \approx -4.6\ \mathrm{m}^{-1}$ for the rotational transition, $\Delta k \approx -54\ \mathrm{m}^{-1}$ for the vibrational transition.

We discard the root ξ_+ since it corresponds to $|E_a/E_s| > 1$ which is physically impossible. We find that ξ_- is a constant that is not dependent on the pumping rate (i.e., the amplitude ratio of the anti-Stokes and Stokes fields is only dependent on their wavelengths and cavity's properties). Eq.(2.104b) can be written in term of ξ_- in the form

$$|E_p| = \sqrt{\frac{\gamma_{cs}}{2G(\delta)\left(1-\xi_-|C_c|\right)}}. \tag{2.107}$$

Comparing with Eq.(2.70), we find that when the Stokes–anti-Stokes coupling is present, the pump light is clamped at a higher value or equivalently, the steady-state Stokes gain $G(\delta)$ is decreased by $(1-\xi_-|C_c|)$ (note that $0 \leq \xi_- \leq 1$ and $0 \leq |C_c| \leq 1$).

From Eq.(2.104a) we can solve for $|E_s|$ and $|E_a|$:

$$|E_s| = \sqrt{\frac{\omega_s k_s}{\omega_p k_p} \frac{\gamma_{ep}|E_{ep}|/|E_p| - \gamma_{cp}}{2G(\delta)[1 - \xi_-^2(k_p + k_s)/(k_p + k_a)]}}, \tag{2.108}$$

$$|E_a| = \xi_-|E_s|. \tag{2.109}$$

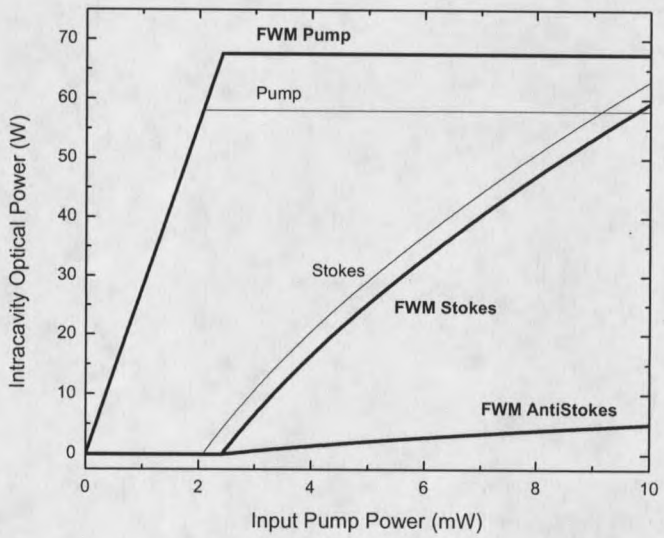

Figure 12 Theoretical plots for the rotational Raman laser (steady-state and zero two-photon-detuning). Thin curves are for the usual Stokes laser while thick curves are when there is four-wave mixing coupling between the Stokes and anti-Stokes. About 8.5% power conversion from Stokes to anti-Stokes, or 3.5% peak power conversion from the input pump to the anti-Stokes can be achieved. Same parameters are used for calculation as in Fig. 11.

Numerical solution

For the general case when the two-photon-detuning $\delta \neq 0$, we numerically solve Eqs. (2.98) using MATHEMATICA [35].

We numerically solve Eqs. (2.98) for the rotational transition pumped by a 792 nm laser (Stokes: 830 nm, anti-Stokes: 757 nm). We choose the rotational instead of a vibrational transition because (1) the rotational transition is easier to be phase-matched (see Fig. 10); and (2) high-finesse mirror coating at wavelengths of the pump, the rotational Stokes and anti-Stokes is easier (see Chapter 4). Therefore generating a cw rotational anti-Stokes beam is easier and our numerical calculation is more practical. The rotational Raman gain and the linewidth used for the numerical calculation are $\alpha_g = 0.5 \times 10^{-9}$cm/W (line-center value for 10 atm H_2 at 25°C)[4, 5, 6] and $\gamma_{abv}/2\pi = 500$ MHz (HWHM; for 10 atm H_2 at 25°C)[7]. The following cavity parameters are used: $R = 0.9999$ (mirror reflectance) and $A = 30 \times 10^{-6}$ (mirrors' power loss) for both mirrors at all three wavelengths; $L = 7.62$ cm (cavity length); $r = 50$ cm (mirrors' radius of curvature) for both mirrors. In addition, we choose the reference frequency $\omega_{p(s,a)} = \omega_{cp(s,a)}/n_{p(s,a)}$ to simplify the calculation.

The first time-dependent result is given in Fig. 13. Assuming the input pump power is four times the line-center threshold (= 2.4 mW), the field amplitudes of the pump, the Stokes, and the anti-Stokes waves are calculated as functions of time. We convert them into optical powers using Eq. (2.81) and then plot in Fig. 13. Three cases of different Raman detunings (all at 4 times the line-center threshold) are calculated and plotted. It can be seen that, as the laser is detuned away from the Raman

resonance by 800 MHz, it turns on smoothly and slowly due to the weaker pumping rate (the threshold increases as detuned away); whereas when the laser is on or near the Raman resonance (now it is pumped harder), there are dramatic dynamics before the steady state for all three waves.

We are interested in steady-state tuning characteristics — optical powers of the three fields as functions of the two-photon-detuning. Although it is difficult to do the analytic steady-state solutions in the case of $\delta \neq 0$, we can obtain them from the time-dependent numerical results (i.e., picking the values after the steady-state is reached). Using this method, the steady-state tuning results are plotted in Fig. 14.

Since we directly solve the complex field equations, besides field amplitudes we also obtain the solutions to the phases. Fig. 15 shows that, at steady state, the phases of the three fields change linearly with time. The slopes of the linear changes give the amounts of frequency-pulling. Fig. 16 plots the steady-state frequency-pullings of the three fields as functions of the two-photon-detuning after we calculate the slopes in Fig. 15.

Although Fig. 15 shows that the individual phases of the three fields change linearly with time at steady-state, we find that the phase difference, $\Delta\phi = 2\phi_p - \phi_s - \phi_a$, will settle down to a constant after the steady state is reached (like the field amplitudes), see Fig. 17. We see that only when the two-photon-detuning is zero, $\Delta\phi = \pi$; when we detune away from the Raman line-center, $\Delta\phi$ is close to, but not exactly equal to π. Going back to Eqs. (2.100) and (2.101), this means that only

when the two-photon-detuning $\delta = 0$, the equations of the amplitudes and the phases are de-coupled and the analytic solution is possible.

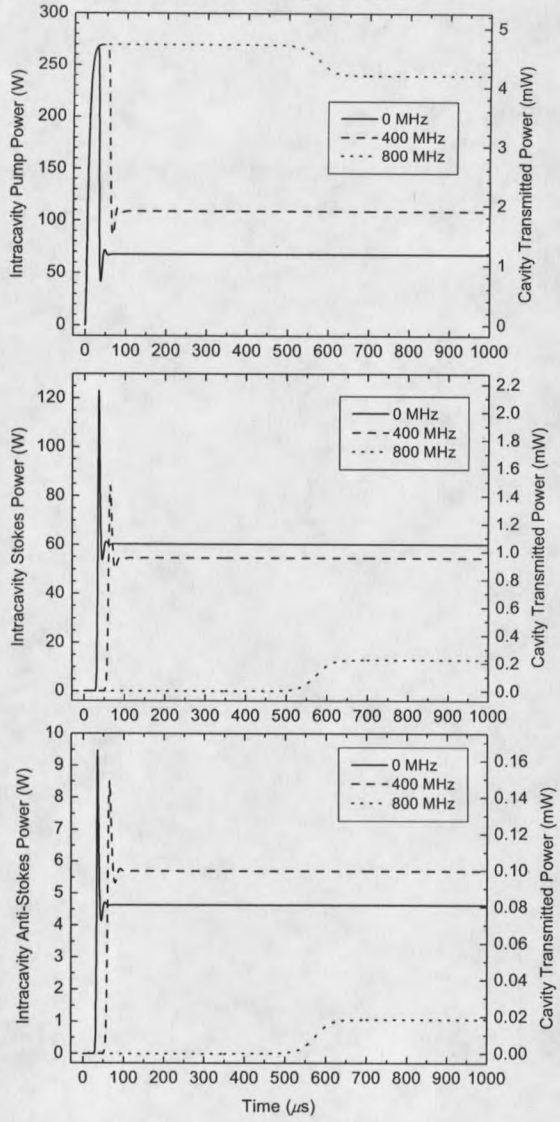

Figure 13 Numerical simulation of the "turn-on" behavior in a cw rotational Raman laser with anti-Stokes emission at different Raman detunings. The pump (top), Stokes (middle), and anti-Stokes (bottom) powers are plotted as functions of time. They are all pumped at 4 times the line-center threshold (= 2.4 mW). The solid line, the dashed line, and the dotted line are when the two-photon-detuning $\delta/2\pi = 0$ MHz, = 400 MHz, and = 800 MHz respectively. The left horizontal axis is the intracavity spatial peak power and the right axis is the cavity transmitted power (single end).

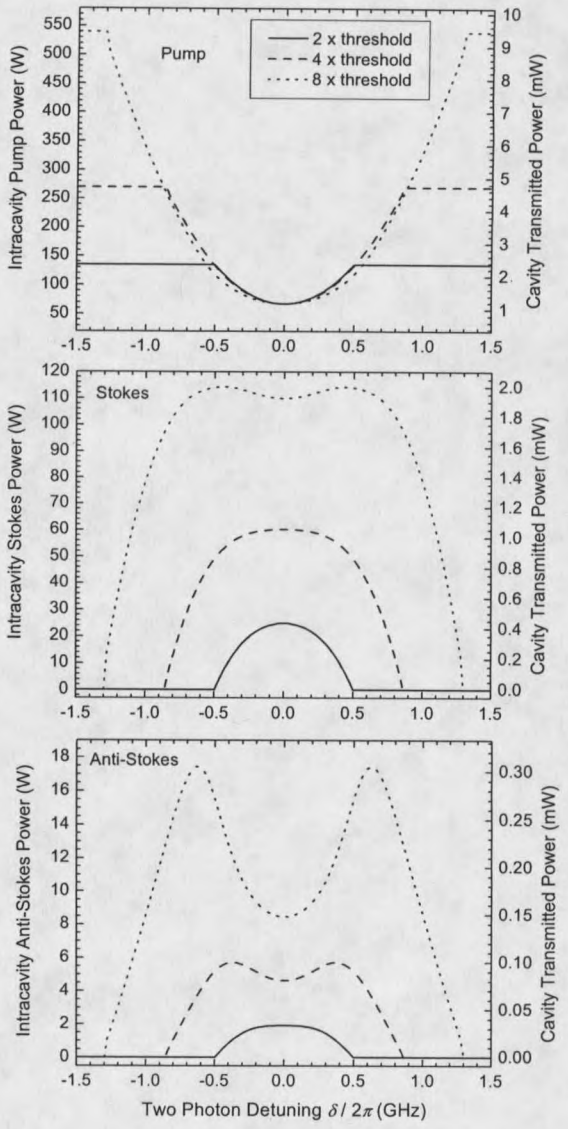

Figure 14 The steady-state powers of pump (top), Stokes (middle), and anti-Stokes (bottom) are numerically calculated as functions of the two-photon-detuning. The solid line, the dashed line, and the dotted line are when the pumping-rate is equal to $2\times$, $4\times$, and $8\times$ the line-center threshold ($= 2.4$ mW) respectively. The left horizontal axis is the intracavity spatial peak power and the right axis is the cavity transmitted power (single end).

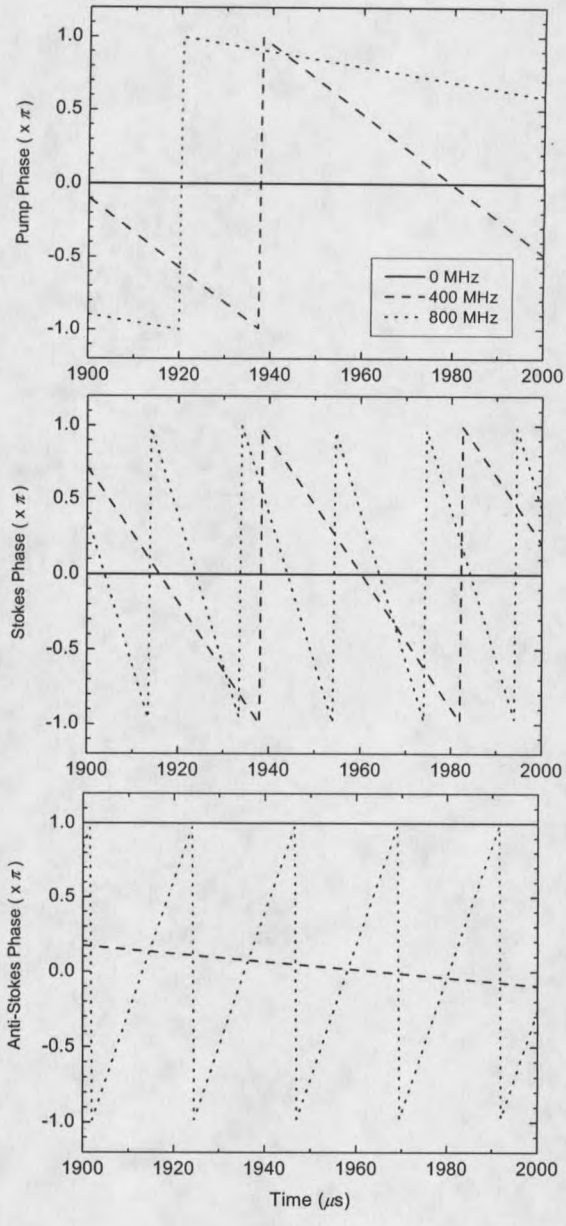

Figure 15 The numerically calculated steady-state phase evolutions in a cw rotational Raman laser with anti-Stokes emission at different Raman detunings. The pump (top), the Stokes (middle), and the anti-Stokes (bottom) phases are plotted as functions of time. They are all pumped at 4 times the line-center threshold ($= 2.4\,\mathrm{mW}$). The solid line, the dashed line, and the dotted line are when the two-photon-detuning $\delta/2\pi = 0\,\mathrm{MHz}$, $= 400\,\mathrm{MHz}$, and $= 800\,\mathrm{MHz}$ respectively.

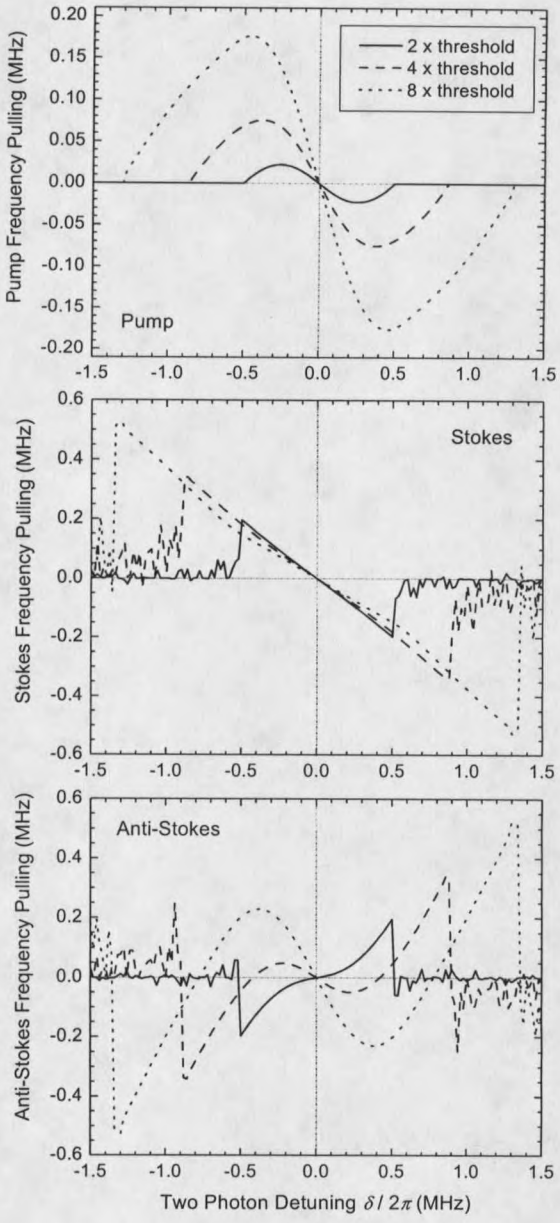

Figure 16 The numerically calculated steady-state frequency-pullings of pump (top), Stokes (middle), and anti-Stokes (bottom) as functions of two-photon-detuning. The solid line, the dashed line, and the dotted line are when the pumping-rate is equal to $2\times$, $4\times$, and $8\times$ the line-center threshold ($=2.4\,\mathrm{mW}$) respectively. The random noise-like curves are when the laser is below threshold.

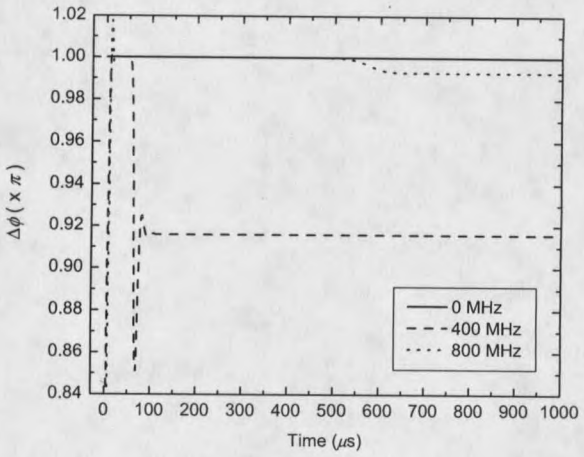

Figure 17 The numerically calculated phase difference, $\Delta\phi = 2\phi_p - \phi_s - \phi_a$, as a function of time. The solid line, the dashed line, and the dotted line are when the two-photon-detuning $\delta/2\pi = 0$ MHz, $= 400$ MHz, and $= 800$ MHz respectively. They are all pumped at 4 times the line-center threshold ($= 2.4$ mW).

Furthermore, we collect the steady-state values of $\Delta\phi$ from the results shown in Fig. 17 and then plot these values in Fig. 18.

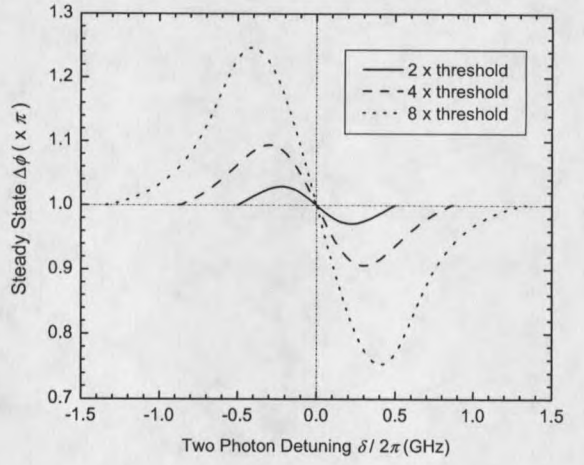

Figure 18 The numerically calculated steady-state values of the phase difference, $\Delta\phi = 2\phi_p - \phi_s - \phi_a$, as a function of two-photo-detuning. The solid line, the dashed line, and the dotted line are when the pumping-rate is equal to $2\times$, $4\times$, and $8\times$ the line-center threshold ($= 2.4$ mW) respectively.

Bad news: the dispersion

So far, using the triple-resonance cavity enhancement to generate cw anti-Stokes light seems to be a promising new method of frequency up-conversion: the threshold is below 10 mW and the power conversion efficiency can reach 3.5% for the rotational transition (see Fig. 12). This only requires the cavity mirrors to have a reflectance of 0.9999 and absorption of 30 parts per million — practically realizable in the mirror coating with a wavelength bandwidth of 80 nm (to cover the range from the rotational Stokes to anti-Stokes in H_2). However, the above prediction is based on the theoretical work assuming that all three fields are resonant with the cavity. The question is: can this condition be realized in reality?

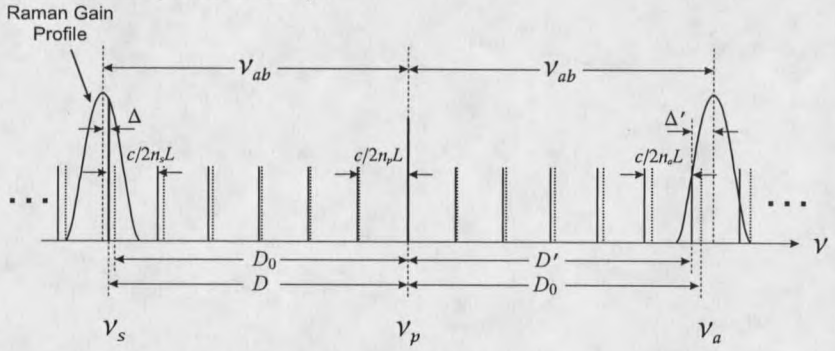

Figure 19 Illustration of (single-photon) dispersion effect in a high-finesse Raman cavity. Solid vertical lines represent actual cavity longitudinal modes (the taller and thicker solid lines means the oscillating modes); dotted vertical lines are "conceptual" and are drawn equally spaced — they are the longitudinal modes assuming that the intracavity refractive index is a constant n_p. Using these modes as a reference, the actual cavity mode-spacings will be larger at lower frequencies and smaller at higher frequencies. ν_{ab} is the Raman shift; Δ is the Raman detuning of the lasing Stokes mode; Δ' is the detuning of the anti-Stokes resonance. The anti-Stokes mode cannot oscillate unless $\Delta' = -\Delta$.

Using Fig. 19, let us analyze if all three fields can be simultaneously resonant

with the cavity. Because of the frequency-dependent refractive index in H_2 (i.e., dispersion), the cavity longitudinal mode-spacing (or free-spectral-range) $c/2nL$ is also frequency dependent. Specifically, we have $c/2n_sL > c/2n_pL > c/2n_aL$ since $n_s < n_p < n_a$. If, starting from the pump frequency ν_p we move along the frequency axis to the left, then the actual cavity modes (solid lines) will be seen ahead of the reference pump modes (dashed lines). When we reach the Stokes frequency range ν_s, the pump modes have accumulated a distance of D_0:

$$D_0 = N_c \times \frac{c}{2n_pL}, \tag{2.110}$$

where N_c is the total number of cavity longitudinal modes in the Raman shifting range of ν_{ab}; for our 3 inch cavity and the rotational transition $\nu_{ab} = 586.9\,\mathrm{cm}^{-1}$, $N_c = 8956$ (Fig. 19 only shows 7 modes for illustration). Meantime, the actual cavity modes have accumulated a distance of D:

$$\begin{aligned} D &= \frac{c}{2(n_p - \Delta n)L} - \frac{c}{2(n_p - 2\Delta n)L} - \cdots - \frac{c}{2(n_p - N\Delta n)L} \\ &= \frac{c}{2L}\sum_{m=1}^{N_c} \frac{1}{n_p - m\Delta n}, \end{aligned} \tag{2.111}$$

where Δn is the refractive index change per free-spectral-range (we assume the dispersion between ν_s and ν_p is linear, see Fig. 20).

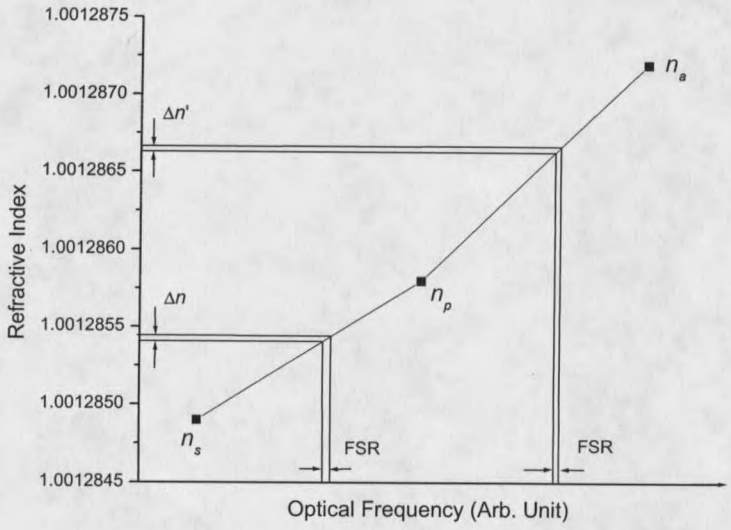

Figure 20 Dispersion in Raman cavity. Refractive index values are for rotational Raman transition (pump = 792 nm, Stokes = 830 nm, and anti-Stokes = 757 nm) in 10 atm H_2 at room temperature. Δn and $\Delta n'$ are the average index changes per free-spectral-range.

Similarly, at the anti-Stokes side,

$$D' = \frac{c}{2L} \sum_{m=1}^{N_c} \frac{1}{n_p + m\Delta n'}. \tag{2.112}$$

Therefore, instead of having a two-photon-detuning Δ, the anti-Stokes resonance now has a detuning Δ' from the Raman gain line-center and from the above formulas we have

$$\begin{aligned} |\Delta'| - |\Delta| &= (D - D_0) + (D_0 - D') \\ &= \frac{c}{2L} \sum_{m=1}^{N_c} \left(\frac{1}{n_p - m\Delta n} - \frac{1}{n_p + m\Delta n'} \right). \end{aligned} \tag{2.113}$$

This is the amount of frequency offset brought by the dispersion; the anti-Stokes cavity resonance cannot oscillate unless this offset equals zero (i.e., $\Delta' = -\Delta$). Table 1 gives several values of this offset in various conditions calculated by Eq. (2.113).

Type of transition	H_2 pressure	Refractive indexes	Dispersion Offset
Rotational $\lambda_p = 792$ nm $\lambda_s = 830$ nm $\lambda_a = 757$ nm	10 atm	$n_s = 1.0012849$ $n_p = 1.0012858$ $n_a = 1.0012872$	20.2 MHz
	1 atm	$n_s = 1.0001285$ $n_p = 1.0001286$ $n_a = 1.0001287$	2.03 MHz
Vibrational $\lambda_p = 792$ nm $\lambda_s = 1180$ nm $\lambda_a = 596$ nm	10 atm	$n_s = 1.0012765$ $n_p = 1.0012858$ $n_a = 1.0012956$	168 MHz
	1 atm	$n_s = 1.0001276$ $n_p = 1.0001286$ $n_a = 1.0001296$	16.8 MHz

Table 1 Calculated frequency-offset values of the anti-Stokes cavity resonance caused by the dispersion (all for room temperature). Refractive indexes of H_2 are estimated by curve-fitting the published values given in reference [1], page 6-95.

From Table 1, we see that the (single-photon) dispersion results in frequency-offsets on the anti-Stokes cavity modes that are larger than the usual linewidth of the high-finesse cavity ($\sim 10\,\text{kHz} - 1\,\text{MHz}$). One might think that the frequency-pullings induced by the two-photon dispersion (see Fig. 16) can compensate these frequency-offsets by appropriately detuning away from the Raman line-center. Unfortunately, the two-photon frequency-pullings are still too small ($< 1\,\text{MHz}$). Therefore the anti-Stokes modes are not able to oscillate in the cavity; in other words, the triple-resonance condition we relied on to derive the theory cannot be reached.

However, we have noted that it is possible to fabricate broadband, high-reflectivity, and dispersion-compensating mirrors [36]. These so-called "chirped" mirrors allow for longer wavelengths penetrating deeper into the mirror. Therefore this is a way for us

to compensate for the dispersion so that the pump, Stokes and anti-Stokes fields can have the same effective cavity length, or the same mode-spacing. If this is true, then in Fig. 19, the Stokes and anti-Stokes modes will be symmetrically positioned away from the pump mode in frequency, and the triple-resonant condition can be achieved.

This entire analysis on the dispersion effect was considered by Roos [24] and is presented here under his permission.

CHAPTER 3

DIODE-PUMPED CW VIBRATIONAL RAMAN LASER

We present in this chapter the experimental achievements of the diode-pumped cw vibrational Raman laser.

System Overview and Characteristics

Vibrational Raman transition in H_2

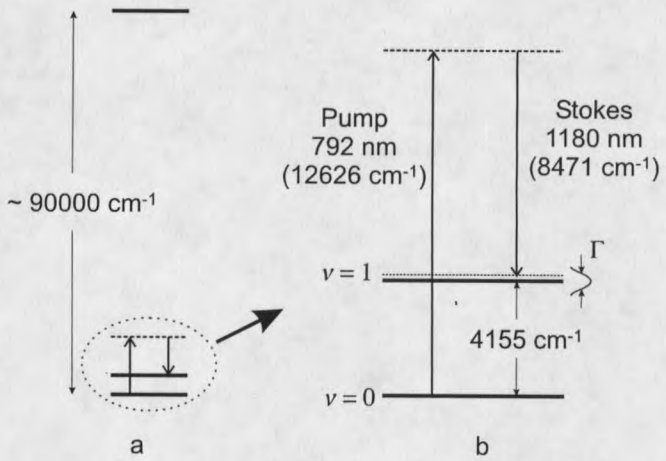

Figure 21 Energy level diagram for the cw vibrational Raman laser in H_2. Spectral distances between levels and laser frequencies are drawn to scale. a, Three levels from bottom to top are (thick solid lines): the ground state, the first vibrational state, and the first excited electronic state. Distance between the ground state and the first electronic state is about 90,000 cm^{-1}. b, Zoomed-in diagram showing the two-photon Raman process. The incident pump photon transfers population from the ground state (the vibrational quantum number $v = 0$) to the vibrational state $v = 1$ producing a Stokes photon with a frequency shift of 4155 cm^{-1}.

We use diatomic hydrogen gas (H_2) at room temperature as the Raman gain

medium. The vibrational Raman transition in H_2 has a frequency shift of 4155 cm^{-1} from $v = 0$ to $v = 1$ level (labeled as $Q_{01}(1)$[1]), as shown in Fig. 21. There are other vibrational transitions as well. But they have less gain than the $Q_{01}(1)$ and these Stokes wavelengths are not covered by the cavity's high-finesse bandwidth so will not lase in our cw Raman system.

The vibrational Raman gain linewidth was studied by Bischel and Dyer [3]. They gave a best-fit formula for the FWHM Raman linewidth in MHz^2 for temperature between 77-500 K, densities of 1-50 amagats[3]:

$$\Gamma(\rho, T) = \frac{309}{\rho}\left[\frac{T}{298}\right]^{0.92} + [51.8 + 0.152(T - 298) + 4.85 \times 10^{-4}(T - 298)^2]\rho, \qquad (3.1)$$

where ρ is the H_2 density in amagats, T is the temperature in Kelvin. We plot linewidth vs. pressure at the temperature of 298 K in Fig. 22.

---

[1] In $Q_{01}(1)$, Q denotes a pure vibrational Raman transition; the subscript 01 means from $v = 0$ to $v = 1$ level; and the number 1 in the parenthesis tells the initial rotational J level (since this is a pure vibrational transition, the initial and final J are equal)

[2] In this and the next chapters, the units of all the quantities associated with frequency or rate are Hz instead of rad/sec we used in the last chapter. Consequently the notations are changed from the last chapter (in parentheses): ν (ω) for optical frequency; Γ ($2\gamma_{ab}$) for FWHM Raman linewidth; Δ (δ) for two-photon-detuning, etc.

[3] Amagat is a density unit for gas. It is defined as the molar density at 0°C and 1 atm pressure. For H_2, 1 amagat $= 4.4587 \times 10^{-5}$ mole/$cm^3 = \rho_A$. For an actual gas,

$$P/\rho = A + B\rho_A + C\rho_A^2 + \cdots,$$

where P is pressure in atm, ρ is the molar density in amagat, and A, B, and C are constants. For H_2 at 25°C, $A = 1.09086$, $B = 0.6606 \times 10^{-3}$ and $C = 2.521 \times 10^{-6}$. Thus for converting between pressure in atm and density in amagat for H_2 at 25°C, approximately 1 amagat $\leftrightarrow$ 1.091 atm, or 1 atm $\leftrightarrow$ 0.917 amagat (at 0°C, approximately 1 amagat $\leftrightarrow$ 0.999 atm). Reference: [1, page 4-158,165].

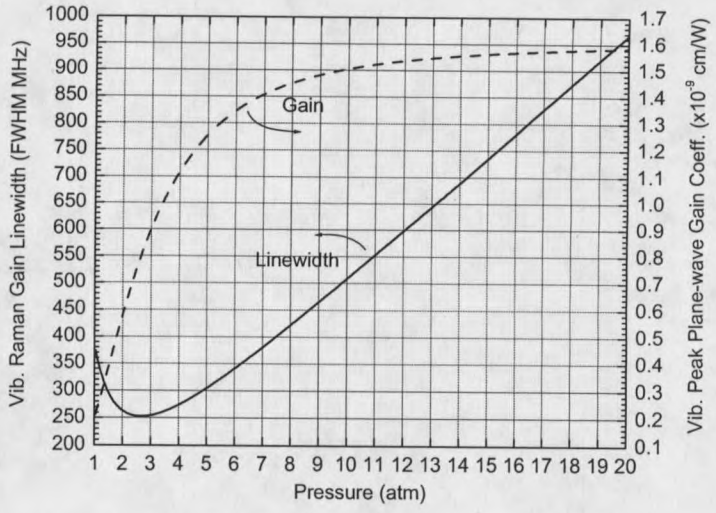

Figure 22 Vibrational Raman gain linewidth and peak plane-wave gain coefficient in H_2 as functions of pressure at 25°C. A pump wavelength of 792 nm is used in calculating the gain coefficient.

From Fig. 22, we see that at 298 K, above a high-pressure limit of 5~6 atm, the gain linewidth roughly linearly increases with the pressure. This is mainly caused by homogeneous pressure-broadening (the Raman coherence is damped by collisional dephasing) and the line-shape is close to a pure Lorentzian. When the pressure is neither high nor low (1 to 5 atm in Fig. 22), the linewidth is at a minimum. This is caused by the effect known as Dicke narrowing [37] or motional narrowing [38]. In this pressure region, the mean-free-path is comparable or a little less than a wavelength; the Doppler effect is restrained but the collisional dephasing is also not strong. Hence the linewidth is narrow in this region. Below a low-pressure limit of $\sim$ 1 atm (not shown in Fig. 22), the gain linewidth will not be dependent on pressure. That is

the Doppler-broadened (inhomogeneous) region and the line-shape is close to a pure Gaussian.

The plane-wave Raman gain coefficient was measured by Bischel and Dyer [2] and a empirical formula to calculate the peak Raman gain as a function of wavelength and density at room-temperature (298 K) was given by

$$\alpha_g = 9.37 \times 10^6 \times \frac{52\rho}{\Gamma}\frac{K_B}{0.658}(\nu_p - 4155) \times (7.19 \times 10^9 - \nu_p^2)^{-2}, \qquad (3.2)$$

where ρ is the density in amagats, Γ is the Raman linewidth given by Eq. (3.1), K_B is the Boltzmann population factor equal to 0.658 at 298 K for the $J = 1$ level in H_2, and ν_p is the pump laser frequency in cm^{-1}. We plot this gain coefficient as a function of H_2 pressure in Fig. 22 (pump wavelength: 792 nm). Above a high-pressure limit of 7~8 atm, the peak Raman gain is nearly independent of pressure.

Threshold and steady-state power dependence

The power dependence equations given in this section were originally developed by Roos in Ref. [39].

The Stokes lasing threshold has been calculated in Chapter 2. When the input pump power P_{ep} is equal to or larger than

$$\begin{aligned} P_{th} &= \frac{\pi bc}{8\omega_p \mu_0 L}\frac{1}{G(\delta)}\frac{\left(\ln\sqrt{R_{1p}R_{2p}}\right)^2}{4T_{1p}}\left(-\ln\sqrt{R_{1s}R_{2s}}\right) \\ &= P_0\frac{\left(\ln\sqrt{R_{1p}R_{2p}}\right)^2}{4T_{1p}}\left(-\ln\sqrt{R_{1s}R_{2s}}\right) \end{aligned} \qquad (3.3)$$

there will be Stokes generation (for notations please see Chapter 2). Here P_0 is defined

by

$$\mathrm{P}_0 = \frac{\lambda_p + \lambda_s}{2\alpha_g \arctan(L/b)}, \tag{3.4}$$

which has a unit of power. Since the cavity finesse is related to the mirror reflectance R (assuming identical front and back mirrors) by

$$\mathcal{F} = \frac{\pi\sqrt{R}}{1-R}, \tag{3.5}$$

the threshold can be written in the form

$$\mathrm{P}_{\mathrm{th}} \approx \frac{\pi^2}{4}\frac{\mathrm{P}_0}{\mathcal{F}_p\mathcal{F}_s} \tag{3.6}$$

when the approximation $R \approx 1$ is used. From this equation, P_0 is approximately the threshold pump power if without the cavity enhancement[4].

From Chapter 2, the spatial peak intracavity powers (at the antinodes of the standing-wave), or four times the cavity circulating powers, are given by

(Intracavity pump:)

$$\Pi_p = \begin{cases} \frac{4T_{1p}}{(1-\sqrt{R_{1p}R_{2p}})^2}\mathrm{P}_{ep}, & \text{if } \mathrm{P}_{ep} < \mathrm{P}_{\mathrm{th}}; \\ \left(-\ln\sqrt{R_{1s}R_{2s}}\right)\mathrm{P}_0, & \text{if } \mathrm{P}_{ep} \geqslant \mathrm{P}_{\mathrm{th}}. \end{cases} \tag{3.7}$$

(Intracavity Stokes:)

$$\Pi_s = \begin{cases} 0, & \text{if } \mathrm{P}_{ep} < \mathrm{P}_{\mathrm{th}}; \\ \frac{\lambda_p}{\lambda_s}\left[2\sqrt{\frac{T_{1p}}{\left(-\ln\sqrt{R_{1s}R_{2s}}\right)}\mathrm{P}_0\mathrm{P}_{ep}} - \left(-\ln\sqrt{R_{1p}R_{2p}}\right)\mathrm{P}_0\right], & \text{if } \mathrm{P}_{ep} \geqslant \mathrm{P}_{\mathrm{th}}. \end{cases} \tag{3.8}$$

---

4 This statement can be justified by reference [33]. It can be seen that for a focused Gaussian pump beam, $\mathrm{P}_0/2$ represents the pump power that gives an unity exponential-gain-coefficient.

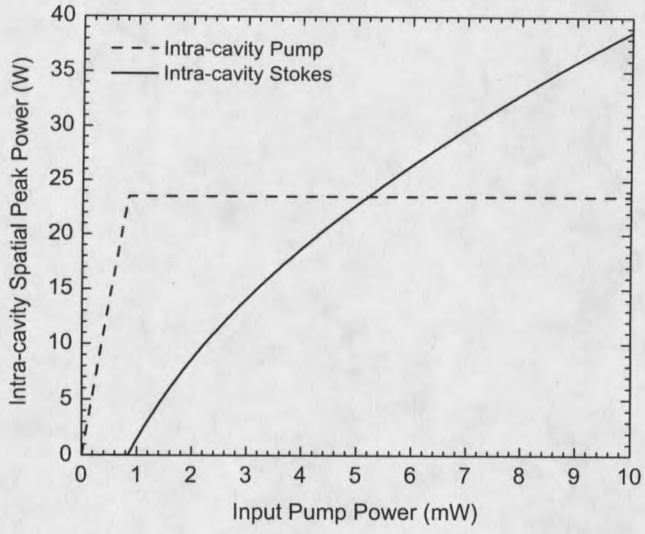

Figure 23 Theoretically calculated intra-cavity pump and Stokes spatial peak powers as functions of input pump power. This is calculated for the vibrational Stokes emission (1180 nm) pumped by 792 nm laser and the Stokes cavity resonance is in the gain line-center. Cavity finesse is assumed to be 31,400 ($R = 0.9999$) at both wavelengths.

In Fig. 23 we plot these two intracavity powers as functions of the input pump power using the following practical parameters: $R_{1p} = R_{2p} = R_{1s} = R_{2s} = 0.9999$ (cavity finesse: 31,400 at both wavelengths), $A_{1p} = A_{2p} = A_{1s} = A_{2s} = 30 \times 10^{-6}$ (mirrors' power loss), $L = 7.62$ cm, $b = 26.5$ cm (or mirrors' radius of curvature = 50 cm), $\lambda_p = 792$ nm, $\lambda_s = 1180$ nm, $\alpha_g = 1.5 \times 10^{-9}$cm/W (line-center value for 10 atm H_2 at 25°C). We see from Fig. 23 the basic behavior of the cw Raman laser: after the threshold is reached the Stokes power starts to grow while the pump power clamps. The threshold in Fig. 23 is about 840 μW; while if without the cavity enhancement the threshold $P_0 \approx 230$ kW. This shows the significance of the cavity enhancement's

ability to lower the Raman threshold.

From Fig. 23 we see that tens of watts is the typical intra-cavity spatial peak power (also circulating power) of the cw Raman laser. Due to the mirrors' absorption, there is heating of the mirrors' coating surfaces. A concern is then whether the intra-cavity laser power can damage the cavity mirrors. Barnes *et al.* has achieved ~ 3 MW/cm^2 intra-cavity intensity without permanent mirror damage [40]. We use mirrors from the same manufacturer (Research Electro-optics) and we estimate that $0.5 \sim 1$ MW/cm^2 is our safety limit given our higher reflectivity (>0.9999 vs. Barnes' 0.9995) and our double-wavelength coating. For the cavity parameters used in the calculations for Fig. 23, the beam areas on the mirror surfaces are approximately 1.1×10^{-3} cm^2 (pump) and 1.7×10^{-3} cm^2 (Stokes). If we take the circulating power to be 100 W, then the light intensities on the mirror surfaces are 91 kW/cm^2 (pump) and 59 kW/cm^2 (Stokes). Therefore we are well within the mirror-damage safety limit.

Knowing the intra-cavity power, the optical power measured just outside the cavity mirrors can be calculated (see Chapter 2) and is given by the following forms:

(Reflected pump:)

$$\mathrm{P}_{1p} = \begin{cases} \left[\sqrt{R_{1p}} - \frac{T_{1p}\sqrt{R_{2p}}}{1-\sqrt{R_{1p}R_{2p}}}\right]^2 \mathrm{P}_{ep}, & \text{if } \mathrm{P}_{ep} < \mathrm{P}_{\mathrm{th}}; \\ \left[\sqrt{\frac{1}{4}T_{1p}\left(-\ln\sqrt{R_{1s}R_{2s}}\right)\mathrm{P}_0} - \sqrt{R_{1p}\mathrm{P}_{ep}}\right]^2, & \text{if } \mathrm{P}_{ep} \geqslant \mathrm{P}_{\mathrm{th}}. \end{cases} \tag{3.9}$$

(Transmitted pump:)

$$\mathrm{P}_{2p} = \begin{cases} \frac{T_{1p}T_{2p}}{\left(1-\sqrt{R_{1p}R_{2p}}\right)^2}\mathrm{P}_{ep}, & \text{if } \mathrm{P}_{ep} < \mathrm{P}_{\mathrm{th}}; \\ \frac{1}{4}T_{2p}\left(-\ln\sqrt{R_{1s}R_{2s}}\right)\mathrm{P}_0, & \text{if } \mathrm{P}_{ep} \geqslant \mathrm{P}_{\mathrm{th}}. \end{cases} \tag{3.10}$$

(Front(back) Stokes:)

$$P_{1s(2s)} = \begin{cases} 0, & \text{if } P_{ep} < P_{th}; \\ \frac{1}{4} T_{1s(2s)} \frac{\lambda_p}{\lambda_s} \left[2\sqrt{\frac{T_{1p} P_0 P_{ep}}{(-\ln \sqrt{R_{1s} R_{2s}})}} + \ln \sqrt{R_{1p} R_{2p}} P_0 \right], & \text{if } P_{ep} \geqslant P_{th}. \end{cases} \quad (3.11)$$

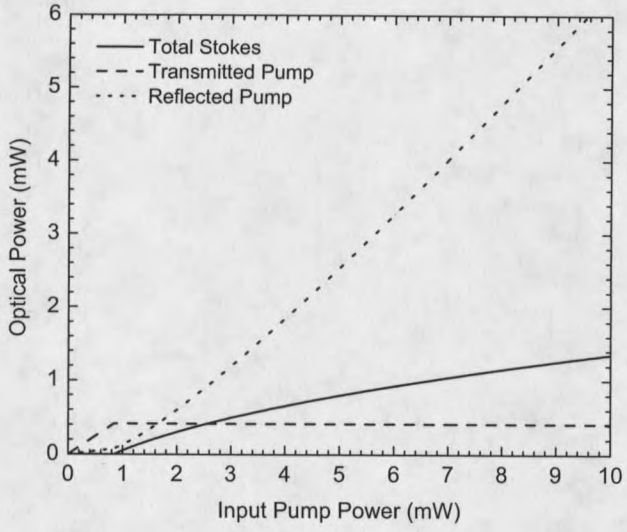

Figure 24 Theoretically calculated optical powers measured outside the cavity as functions of input pump power. The calculation parameters are the same as used in Fig.23. We add the Stokes powers in front and back of the cavity to obtain the total Stokes power.

We plot them as functions of input pump power in Fig. 24 using the same parameters as used in Fig. 23. One can see that the Stokes power grows and the transmitted pump clamps after the threshold; this is the same dependence as with the intra-cavity power. However, the reflected pump power grows quickly as the input pump increases. Certainly this is not a very efficient system in regards to Stokes conversion: a large percent of the pump photons are reflected away from the cavity and cannot contribute to the Stokes conversion. Next we will discuss the method of improving the Stokes conversion efficiency.

Stokes conversion efficiency and cavity impedance-matching

We define a photon conversion efficiency of the cw Raman laser:

$$\eta = \frac{\lambda_s}{\lambda_p} \frac{P_{1s} + P_{2s}}{P_{ep}}. \tag{3.12}$$

Using the same parameters as used in Fig. 23, we plot η as a function of input pump power in Fig. 25.

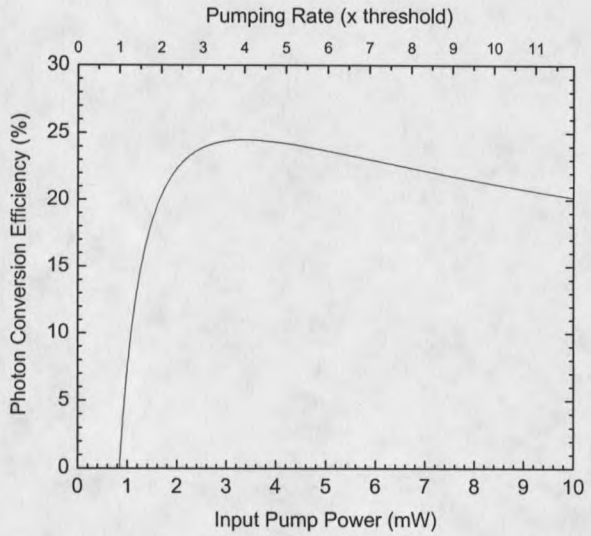

Figure 25 Theoretically calculated photon conversion efficiency as a function of input pump power. The top x axis labels the pumping rate normalized to the laser threshold. Parameters for calculation are the same as used in Fig.23. Photon conversion efficiency reaches the maximum value at 4 times threshold.

The rather low conversion efficiency (maximum value $\sim 25\%$) in Fig. 25 is directly linked to the high reflected pump power as shown in Fig. 24. As shown in Fig. 26, when the input pump laser is resonant with the cavity, the total reflected pump field is a destructive interference between the directly-reflected pump field from the front